Published online: February 11, 2016

Article

SOURCE DATA | TRANSPARENT PROCESS

THE EMBO JOURNAL

ALS-linked protein disulfide isomerase variants cause motor dysfunction

Ute Woehlbier[1,2,3], Alicia Colombo[4,5], Mirva J Saaranen[6], Viviana Pérez[7], Jorge Ojeda[7], Fernando J Bustos[8], Catherine I Andreu[1,2], Mauricio Torres[1,2], Vicente Valenzuela[1,2,9], Danilo B Medinas[1,2,9], Pablo Rozas[1,2], Rene L Vidal[1,9,10], Rodrigo Lopez-Gonzalez[11], Johnny Salameh[11], Sara Fernandez-Collemann[12], Natalia Muñoz[1,9,10], Soledad Matus[1,9,10], Ricardo Armisen[2], Alfredo Sagredo[2], Karina Palma[1,2], Thergiory Irrazabal[1,2], Sandra Almeida[11], Paloma Gonzalez-Perez[11], Mario Campero[13,14], Fen-Biao Gao[11], Pablo Henny[12], Brigitte van Zundert[8], Lloyd W Ruddock[6], Miguel L Concha[1,4,9], Juan P Henriquez[7], Robert H Brown[11,*] & Claudio Hetz[1,2,9,15,**]

Abstract

Disturbance of endoplasmic reticulum (ER) proteostasis is a common feature of amyotrophic lateral sclerosis (ALS). Protein disulfide isomerases (PDIs) are ER foldases identified as possible ALS biomarkers, as well as neuroprotective factors. However, no functional studies have addressed their impact on the disease process. Here, we functionally characterized four ALS-linked mutations recently identified in two major PDI genes, PDIA1 and PDIA3/ERp57. Phenotypic screening in zebrafish revealed that the expression of these PDI variants induce motor defects associated with a disruption of motoneuron connectivity. Similarly, the expression of mutant PDIs impaired dendritic outgrowth in motoneuron cell culture models. Cellular and biochemical studies identified distinct molecular defects underlying the pathogenicity of these PDI mutants. Finally, targeting ERp57 in the nervous system led to severe motor dysfunction in mice associated with a loss of neuromuscular synapses. This study identifies ER proteostasis imbalance as a risk factor for ALS, driving initial stages of the disease.

Keywords amyotrophic lateral sclerosis; ERp57; PDIA1; protein disulfide isomerase

Subject Categories Molecular Biology of Disease; Neuroscience

DOI 10.15252/embj.201592224 | Received 6 June 2015 | Revised 27 December 2015 | Accepted 5 January 2016 | Published online 11 February 2016

The EMBO Journal (2016) 35: 845–865

See also: **N Maharjan & S Saxena** (April 2016)

Introduction

Amyotrophic lateral sclerosis (ALS) is a fatal neurodegenerative disorder affecting motoneurons in the brain and spinal cord (Peters *et al*, 2015). The progressive degeneration of motoneurons leads to loss of motor control resulting in paralysis and death. Approximately 10% of ALS cases are familial (fALS), caused by rare variants in multiple genes (Leblond *et al*, 2014), while the majority is considered sporadic (sALS). Repeat expansion in the intronic region of *C9orf72* and mutations in the gene encoding cytosolic superoxide

1 Biomedical Neuroscience Institute, Faculty of Medicine, University of Chile, Santiago, Chile
2 Program of Cellular and Molecular Biology, Center for Molecular Studies of the Cell, Institute of Biomedical Sciences, University of Chile, Santiago, Chile
3 Center for Genomics and Bioinformatics, Universidad Mayor, Santiago, Chile
4 Program of Anatomy and Developmental Biology, Institute of Biomedical Sciences, University of Chile, Santiago, Chile
5 Department of Pathological Anatomy, Hospital Clínico, University of Chile, Santiago, Chile
6 Biocenter Oulu and Faculty of Biochemistry and Molecular Medicine, University of Oulu, Oulu, Finland
7 Department of Cell Biology, Faculty of Biological Sciences, Millennium Nucleus of Regenerative Biology, Center for Advanced Microscopy (CMA Bio-Bio), Universidad de Concepción, Concepción, Chile
8 Faculty of Biological Sciences and Faculty of Medicine, Center for Biomedical Research, Universidad Andres Bello, Santiago, Chile
9 Center for Geroscience, Brain Health and Metabolism, Santiago, Chile
10 Neurounion Biomedical Foundation, CENPAR, Santiago, Chile
11 Department of Neurology, University of Massachusetts Medical School, Worcester, MA, USA
12 Department of Anatomy, Medical School, Universidad Católica de Chile, Santiago, Chile
13 Department of Neurology and Neurosurgery, Faculty of Medicine, University of Chile, Santiago, Chile
14 Faculty of Medicine, Clínica Alemana, Universidad del Desarrollo, Santiago, Chile
15 Department of Immunology and Infectious Diseases, Harvard School of Public Health, Boston, MA, USA
*Corresponding author. Tel: +1 508 334 1271; E-mail: robert.brown@umassmed.edu
**Corresponding author. Tel: +56 2 978 6506; E-mails: clahetz@med.uchile.cl chetz@hsph.harvard.edu

dismutase 1 (*SOD1*) are the most frequent genetic causes of fALS, accounting for around 50% of fALS cases (Ferraiuolo *et al*, 2011), whereas mutations in TAR DNA-binding protein (*TARDBP*, also known as TDP43) and fused-in-sarcoma/translated-in-liposarcoma (*FUS/TLS*) genes represent about 10% of fALS cases (Ferraiuolo *et al*, 2011). Although the etiology of ALS remains poorly understood, abnormal aggregation and altered proteostasis is a common feature of ALS (Turner *et al*, 2013; Hetz & Mollereau, 2014). As a major compartment for protein folding and quality control, disruption of normal endoplasmic reticulum (ER) function leads to the accumulation of misfolded proteins causing a condition known as ER stress (Walter & Ron, 2011). ER proteostasis disturbance is increasingly recognized as a major driver of neurodegenerative diseases and is also indicated as a common feature of sALS and fALS (Roussel *et al*, 2013; Hetz & Mollereau, 2014). ER stress engages the unfolded protein response (UPR), an adaptive response that orchestrates the recovery of homeostasis and the induction of apoptosis to eliminate irreversibly damaged cells (Hetz, 2012). Recent evidence indicates that ER stress is a salient pathological feature of iPSC-derived ALS motoneurons (Kiskinis *et al*, 2014), and one of the earliest events detected before any denervation is observed (Saxena *et al*, 2009), underlying the differential neuronal vulnerability of motoneurons. Similarly, alteration in the expression of UPR genes was recently reported as a salient feature of ALS patients carrying *C9orf72* mutations (Prudencio *et al*, 2015). Importantly, accumulating studies using genetic or pharmacological manipulation of the UPR have demonstrated a functional role of the pathway in mouse models of ALS (Hetz *et al*, 2013; Oakes & Papa, 2015), highlighting the therapeutic potential for disease treatment.

Proteomic analysis of spinal cord tissue of ALS mouse models uncovered major changes in the levels of two ER stress-inducible foldases of the protein disulfide isomerase (PDI) family, known as PDIA1 (also referred to as PDI or P4HB) and ERp57 (also known as PDIA3 or Grp58) (Atkin *et al*, 2006). This finding was then confirmed in spinal cord tissue (Ilieva *et al*, 2007; Atkin *et al*, 2008) and cerebrospinal fluid (Atkin *et al*, 2008) of sALS patients. Furthermore, the upregulation of PDIA1 and ERp57 protein levels was also identified as the best hits in a proteomic screening for biomarkers in patient blood, suggesting that monitoring these PDIs may be used as indicators for diagnosis and disease progression (Nardo *et al*, 2011). Protein inclusions containing SOD1, TDP-43, and FUS co-localize with PDIA1 in ALS-derived tissue, possibly indicating a physical association between them (Atkin *et al*, 2006, 2008; Honjo *et al*, 2011; Farg *et al*, 2012). Inactivation of PDIA1 by S-nitrosylation has been observed in the spinal cord of sALS patients and mouse models of the disease, a modification that may negatively impact motoneuron survival (Walker *et al*, 2010). Interestingly, an intronic variant of the *PDIA1* gene was proposed as a risk factor to develop ALS (Kwok *et al*, 2013; Yang & Guo, 2015). Based on all the evidence linking PDI biology with ALS, we recently screened for possible mutations in *PDIA1* and *ERp57* using exome sequencing and direct targeting sequencing (Gonzalez-Perez *et al*, 2015). We identified rare exonic variants in both genes that were not present or highly infrequent in large sets of control subjects and predicted through the analysis of the available protein structures putative alterations to their function (Gonzalez-Perez *et al*, 2015). However, to date, most data available for addressing the functional impact of PDI to ALS pathogenesis remain correlative and debated (Jaronen *et al*, 2014).

Alteration in PDIs function is emerging as a common factor in many neurodegenerative diseases (Andreu *et al*, 2012). PDIs constitute a large family of foldases comprised of nearly 20 multifunctional members of the thioredoxin superfamily, which are mainly located to the ER, where they catalyze the formation (oxidation), breakage (reduction), and rearrangement (isomerization) of disulfide bonds of proteins that traffic through the secretory pathway (Ellgaard & Ruddock, 2005; Rutkevich & Williams, 2011). Intramolecular and intermolecular disulfide bonds have important consequences for the structure and function of proteins (Feige & Hendershot, 2011), mediating in many cases the generation of protein aggregates in brain diseases (Andreu *et al*, 2012). In addition to their function as foldases, PDIs can also act as molecular chaperones for unfolded/misfolded proteins at the ER (Hatahet & Ruddock, 2009). PDI family members are built by modules of thioredoxin-like catalytic **a** domains and non-catalytic **b** domains. The catalytic **a** domain contains the CXXC active-site motifs that react with thiols of substrate proteins (Appenzeller-Herzog *et al*, 2010). The non-catalytic **b** domains are responsible for substrate recruitment and provide interaction sites for cofactors (Hatahet & Ruddock, 2009; Appenzeller-Herzog *et al*, 2010). PDIA1 was shown to have a central role in oxidative protein folding, since its deletion in mammalian cells results in delayed disulfide bond formation (Rutkevich *et al*, 2010). ERp57 is a component of the calnexin (CNX) and calreticulin (CRT) cycle, where it is responsible, in complex with CNX and/or CRT, for the folding of glycosylated and disulfide bond-containing proteins (Rutkevich & Williams, 2011). Unexpectedly, PDIA1 and ERp57 may be involved in pro-apoptotic mechanisms in the context of Alzheimer's and Huntington's disease models (Hoffstrom *et al*, 2010). Importantly, increasing reports suggest relevant roles of PDI family members beyond assisting protein folding, including cell signaling, protein quality control, redox control, apoptosis, and cell signaling (Turano *et al*, 2011).

Although PDIs are emerging as relevant factors in neurodegenerative diseases including ALS, studies addressing the biological relevance of these foldases to the nervous system are lacking. Here, we characterize in detail the impact of ALS-linked PDI variants to motoneuron function using cellular, biochemical and *in vivo* approaches; in addition, we define for the first time the function of ERp57 in the nervous system. Our results reveal distinct consequences of these mutations to the structure and function of PDIA1 and ERp57, triggering detrimental effects to motoneuron function and connectivity. This study suggests that alterations in PDI biology are a risk factor to develop ALS.

Results

ALS-linked PDI mutants disrupt motoneuron connectivity and function in zebrafish

We recently identified missense variants in PDIA1 and ERp57 in ALS cases, where we highlight p.D292N and p.R300H which are located in the **b′** domain of PDIA1, and p.D217N and p.Q481K in ERp57, which map to the **b′** domain and the catalytic **a′** domain, respectively (Fig 1A). To assess the possible pathological effects of these PDI variants on an *in vivo* setting, we used zebrafish, a validated model for dissecting mechanisms of neurodegeneration in ALS (Kabashi *et al*, 2010; Patten *et al*, 2014). In zebrafish, we were unable to

Published online: February 11, 2016

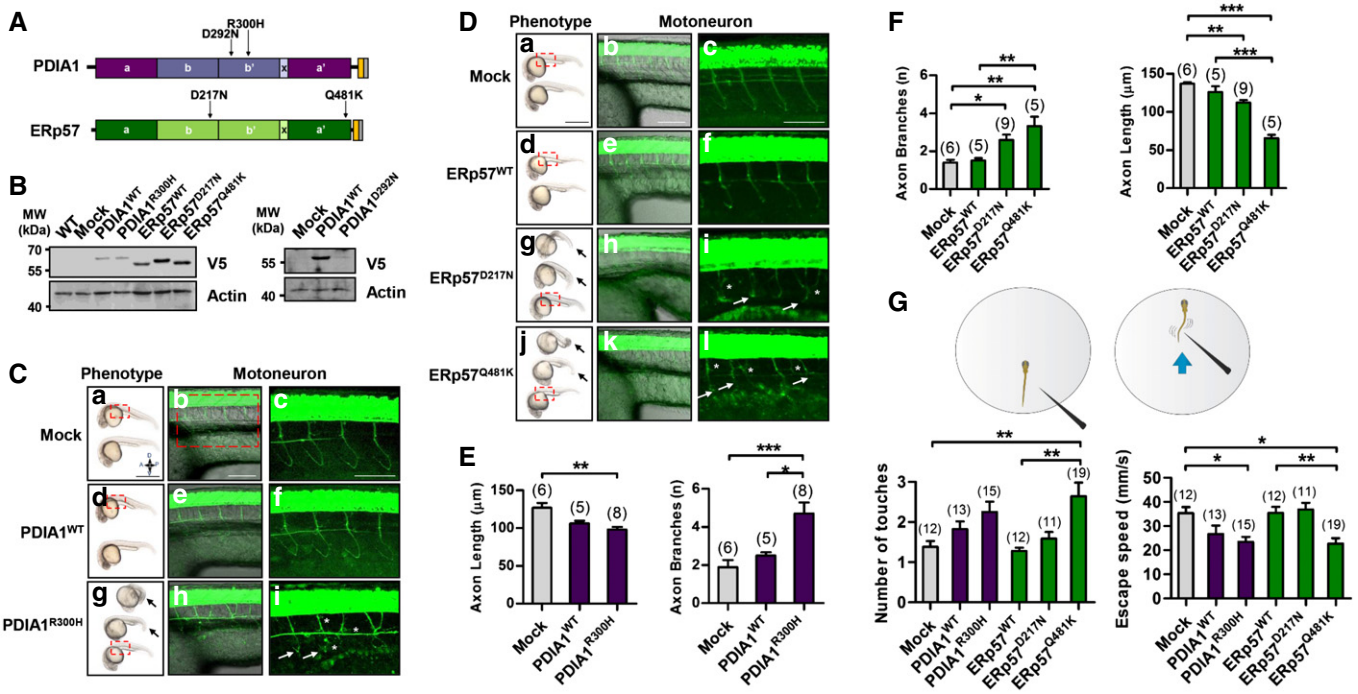

Figure 1. Expression of ALS-linked variants of PDIA1 and ERp57 causes motoneuron dysfunction and impairs neurite outgrowth.

A Location of missense variants of PDIA1 and ERp57 identified in ALS cases. PDI primary structure: catalytic **a** and **a**′ domains containing the active-site motif CXXC sequence (dark purple and dark green), non-catalytic domains **b** and **b**′ containing ligand-binding sites (light purple and light green), and x-linker region (light gray). The constructs used in this study contained a V5-tag (orange) at the C-terminus that was inserted previous to the ER-retention signal (dark gray).

B Expression of PDI variants in zebrafish. Zebrafish embryos at 1–2-cell stage were injected with sense mRNA coding for the indicated PDIs (PDIA1^{WT}, PDIA1^{D292N}, and PDIA1^{R300H}: 200 pg/embryo; ERp57^{WT}, ERp57^{D217N}, and ERp57^{Q481K}: 80 pg/embryo). Protein expression was confirmed by Western blot analysis using anti-V5 antibody in total embryo extracts at 24 h post-fertilization (hpf). Actin was used as a loading control. In the left panel, 80 μg protein extract was used, and in the right panel, 120 μg protein extract was used.

C, D Motoneuron defects induced in zebrafish embryos after expression of the indicated ALS-linked PDI mutants and wild-type controls (PDIA1^{WT} and PDIA1^{R300H}: 80 pg mRNA/embryo; ERp57^{WT}, ERp57^{D217N}, ERp57^{D217N}, and ERp57^{Q481K}: 30 pg mRNA/embryo). The most frequent global phenotypes induced by PDI injection are shown in lateral views of embryos at 24 hpf (left column). Black arrows indicate the presence of curly tail and/or shorter axis phenotypes (see details in Appendix Table S1). Axon motoneuron morphology was visualized using confocal microscopy in lateral views of the trunk region in transgenic *Tg(Huc:Kaede)* zebrafish at 36 hpf (middle and right columns). Images in the right column correspond to magnification views of the rectangular regions depicted in left and middle columns. Asterisks and arrows point to examples of increased axonal branching and reduced axonal length, respectively.

E, F Quantification of motoneuron axon length and axon branching in 36 hpf *Tg(Huc:Kaede)* embryos injected with the indicated PDIA1 (E) and ERp57 (F) mutants.

G Touch-evoked escape responses of 48 hpf zebrafish embryos injected with ALS-linked PDI mutants (Kabashi *et al*, 2009, 2011). The number of touches necessary to evoke an escape response (left) and speed (right, in mm/s) of the escape response was determined for each condition.

Data information: The total number of analyzed embryos is indicated in parenthesis. Experiments of (D–F) were performed in selected animals sharing normal overall embryo morphology and viability, to avoid unspecific effects of axial shortening or curvature in motoneuron morphology and/or animal behavior. Statistical analyses were performed using one-way ANOVA and Bonferroni's *post hoc* tests. Mean ± SEM with only statistically significant *P*-values are shown: $*P \leq 0.05$; $**P \leq 0.01$; $***P \leq 0.001$. Abbreviations: A (anterior), D (dorsal), P (posterior), V (ventral). Scale bars represent 500 μm (C and D: a, d, g, j), 200 μm (C and D: b, e, h, k), and 100 μm (C and D: c, f, i, l).

Source data are available online for this figure.

observe any phenotype caused by PDIA1^{D292N}, probably due to the extremely low level of expression of this mutant in the model at the protein level (Fig 1B and Appendix Table S1). While the majority of embryos expressing wild-type PDIA1 or ERp57 appeared normal in overall morphology at 24 h post-fertilization (hpf), a large fraction of embryos expressing PDIA1^{R300H}, ERp57^{D217N}, and ERp57^{Q481K} showed a striking shortening of the axis and tail curvature (Appendix Table S1; and Fig 1C and D, see arrows), both features previously observed in various zebrafish models of ALS (see examples in Armstrong & Drapeau, 2013; Kabashi *et al*, 2011, 2009). To directly assess the possible effects of ALS-linked mutant expression on motoneuron function, we analyzed motoneuron morphology in animals selected with overall normal appearance using transgenic zebrafish embryos expressing Kaede (a photoactivatable fluorescent protein) in motoneurons under the control of the elav/HuC promoter (Sato *et al*, 2006). Expression of PDIA1^{R300H}, ERp57^{D217N}, and ERp57^{Q481K} did not disrupt the normal spatial organization and number of motoneurons. However, these variants impaired axonal morphology, producing motor axons with abnormal shape, involving a reduction in the length and increased branching (Fig 1C–F). Furthermore, analysis of pre-synaptic (SV2) and post-synaptic (α-bungarotoxin) markers within neuromuscular junctions (NMJ) of myotomes revealed disrupted synapse formation in embryos expressing PDIA1^{R300H} and ERp57^{Q481K} (Fig EV1, see arrows).

We then monitored the possible effects of ALS-linked PDI variants on the motor performance of zebrafish. Consistent with the

alterations observed in motoneuron connectivity, expression of ERp57^{Q481K} and, to a lesser extent, PDIA1^{R300H} induced motor behavioral defects at 48 hpf, as revealed by an increase in the number of stimuli necessary to trigger a touch-evoked escape response (Fig 1G). In addition, a reduction in the speed of the escape response was observed in these experiments when ERp57^{Q481K} and PDIA1^{R300H} were expressed (Fig 1G). These results indicate that expression of the ALS-linked mutants PDIA1^{R300H} and ERp57^{Q481K} disrupted motoneuron connectivity and function in zebrafish, the phenotype resembled those described in other ALS studies in this vertebrate model (see examples in Babin *et al*, 2014; Kabashi *et al*, 2011, 2009).

Expression of PDI variants impairs neuronal outgrowth

To gain insights into the molecular mechanism involved in ALS-linked PDI mutant pathogenesis, we expressed these variants in different motoneuron cell culture systems. First, we transiently transfected the murine motoneuron cell line NSC34 with wild-type PDIs or the four PDI variants alone. We calibrated the system to obtain low overexpression levels compared with endogenous levels of PDIA1 or ERp57 (Fig 2A). Based on our studies with disrupted neuronal branching *in vivo*, we induced differentiation for 24 h by serum starvation followed by the morphological analysis of GFP-positive cells. Unexpectedly, expression of wild-type PDIA1 and ERp57 resulted in marked enhancement of neurite outgrowth (Fig 2B). This effect was lost when PDIA1 or ERp57 mutants were expressed (Fig 2B), suggesting that these mutations abolish the neurite-extending function of the wild-type proteins. In addition, expression of PDI mutants reduced the percentage of NSC34 cells with neurites (Fig 2C). However, no neurotoxicity of mutant PDIs was observed when NSC34 cell viability was analyzed (Appendix Fig S1A).

We then generated primary motoneurons cultures derived from the spinal cord of rat embryos followed by morphological analysis. In these experiments, motoneurons expressing wild-type PDIA1 or ERp57 showed a robust enhancement of dendritic outgrowth, whereas mutant PDIs completely lost this activity, showing a decrease in the length of dendritic branches when compared with wild-type PDIA1 and ERp57 (Fig 2D). These effects were recapitulated when we quantified the length of primary, secondary and tertiary neurites (Appendix Fig S1B). Again, no neuronal death was detected in these assays upon transient expression of mutant PDIs (Appendix Fig S1C).

We then addressed the possible impact of ALS-linked PDI mutants on neurite outgrowth in human motoneurons derived from the human embryonic stem cell line HuESC 3 Hb9::GFP, by expressing PDI variants using lentiviral-mediated transduction (Appendix Fig S1D). We confirmed our findings in human motoneurons, observing that these mutants also reduced the ability of PDIs to enhance neurite outgrowth (Fig 2E). These observations are consistent with recent findings indicating that a major phenotype of ALS-derived human motoneurons carrying well-described genetic mutations is the reduction of dendritic branching (Matus *et al*, 2014).

Based on the observation of increased neurite outgrowth in cells overexpressing the wild-type form of PDIA1 or ERp57, we then monitored the contribution of the endogenous proteins to the process. To this end, we stably transduced NSC34 cells with lentiviruses expressing shRNAs against PDIA1 and ERp57 mRNAs (Appendix Fig S1E). Remarkably, we observed a significant reduction in the number of cells bearing neurites after differentiation (Fig 2F). Together, our results suggest that ERp57 and PDIA1 have an important function in enhancing neuronal outgrowth and that the ALS-linked PDI variants characterized here adversely affect dendritic extension and connectivity.

ALS-linked PDI mutants do not affect the susceptibility of cells to ER stress

PDIs represent an important group of ER stress-responsive genes that are thought to contribute to the recovery of proteostasis downstream of the UPR. To explore the possible impact of ALS-linked PDIs identified here to the physiology of the ER, we first analyzed their subcellular distribution. NSC34 cells were co-transfected with V5-tagged PDI variants together with a KDEL-RFP construct to assess their subcellular distribution. In addition to showing a normal co-localization with the ER marker, mutant PDIA1 or ERp57 did not alter the morphology of this organelle (Appendix Fig S2).

We next analyzed whether the expression of ALS-linked PDIs alters the susceptibility of cells to ER stress. NSC34 cells expressing mutant or wild-type PDIA1 and ERp57 were treated with the ER stress agent tunicamycin (an inhibitor of N-glycosylation). The expression of the UPR mediators XBP1 and ATF4, or the upregulation of the ER chaperone BiP, was not enhanced in cells expressing ALS-linked PDIs compared to the wild-type forms (Fig EV2A). We also monitored the viability of cells undergoing ER stress. Treatment of cells with different doses of thapsigargin (an inhibitor of the SERCA pump) leads to equivalent percentages of cell death in cells expressing wild-type or mutant PDIs as monitored by propidium iodide staining (Fig EV2B). Similar results were obtained when cells were treated with tunicamycin (Fig EV2C). These results are consistent with our recent findings indicating that ERp57 does not affect the susceptibility of cells to undergo ER stress (Torres *et al*, 2015). Finally, to monitor the physiological status of the ER with an additional parameter, we determined the rate of secretion of two proteins that are synthetized through the secretory pathway. NSC34 cells were co-transfected with a BDNF-GFP expression construct together with our PDI variants. Western blot analysis of the supernatant of cells after 18 or 42 h of transfection indicated no alterations in the rate of BDNF-GFP secretion (Fig EV2D). Similar results were obtained when we measured the levels of progranulin in the cell culture media using ELISA, where only PDIA1^{R300H} showed a minor reduction in progranulin secretion (Fig EV2E). Taken together, these results suggest that the expression of ALS-linked PDIs do not trigger clear alterations to the homeostasis of the ER.

ALS-linked PDIA1 mutants have altered enzymatic activity

To define the possible molecular defects underlying the pathogenicity of the ALS-linked PDI variants, we undertook several cellular and biochemical approaches to assess key aspects of PDI biology. To investigate the effects of the mutations on the functionality of the PDIs, we expressed the four PDI mutants in NSC34 cells. In absence of reducing agents, we observed the appearance of protein complexes after Western blot analysis, reflecting increased mixed disulfide bond formation for PDIA1^{D292N}, ERp57^{D217N}, and ERp57^{Q481K} compared to the respective wild-type proteins (Figs 3A

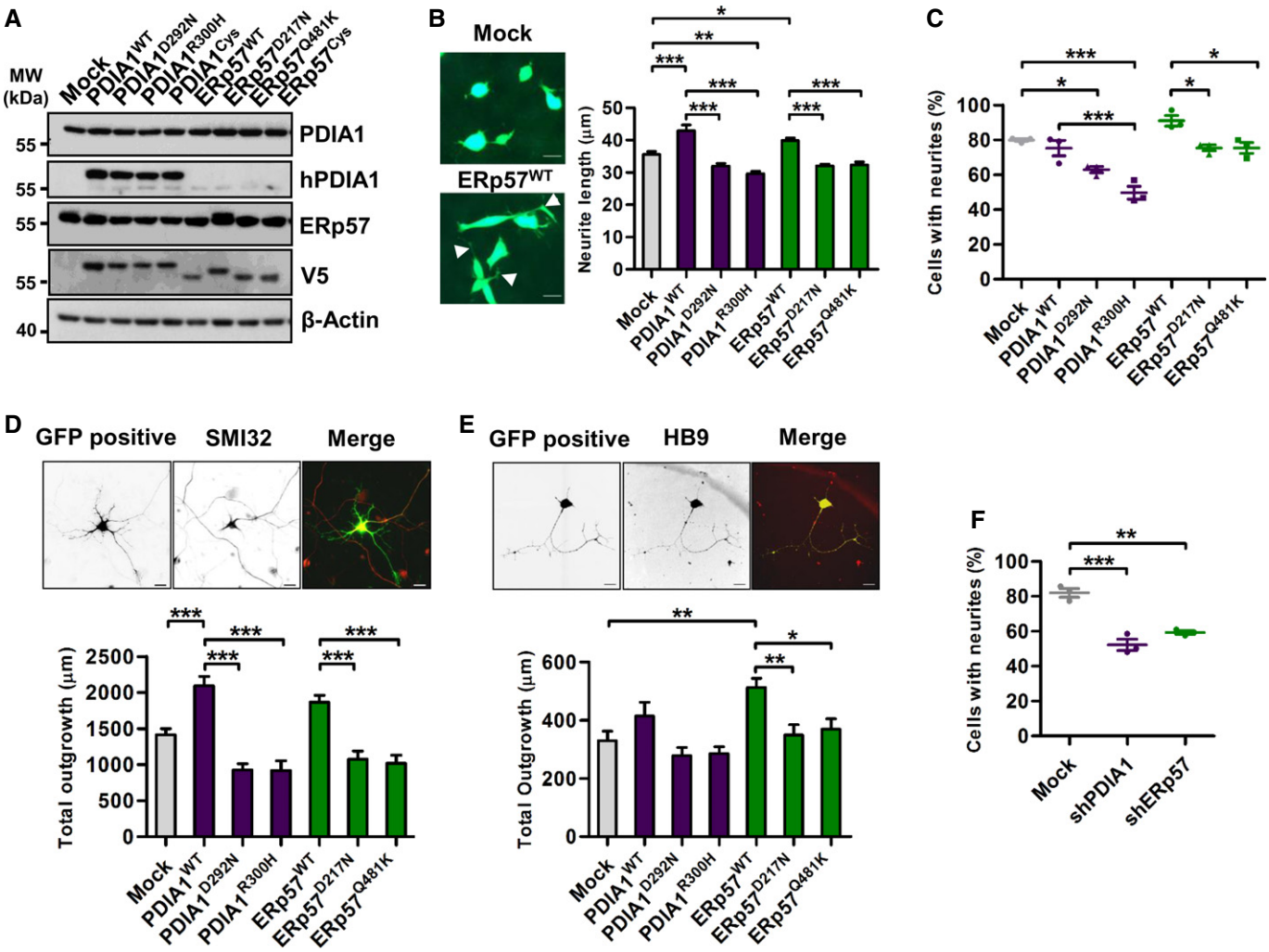

Figure 2. Motoneuron morphology upon expression of ALS-linked PDI variants.

A NSC34 cells were transiently transfected with expression vectors for V5-tagged wild-type and mutant PDIs. After 48 h, overexpressed PDI variants were assessed under reducing conditions in an 8% SDS–PAGE. An antibody detects total PDIA1 (endogenous mouse PDIA1 and exogenous human V5-tagged PDIA1) (first panel). A second antibody detects only human PDIA1, therefore only V5-tagged PDIA1 appears (second panel). A mouse- and human-specific antibodies were used to detect total ERp57 (third panel). Anti-V5 was used to detect the exogenous PDI variants. Anti-β-actin was used as a loading control.

B, C NSC34 cells were transiently transfected with the indicated PDI constructs together with a GFP expression plasmid. Cells were then differentiated for 24 h in Neurobasal medium containing B27 supplement to induce cell differentiation. Increased neurite outgrowth is indicated with white arrow heads. (B) Quantification of the average primary neurite lengths was performed, all cells from three independent experiments were compiled. A minimum of 100 cells per experiment were analyzed. In addition, (C) the percentage of cells with neurites was quantified in the three independent experiments (right panel).

D Primary rat ventral spinal cord neurons were prepared and after 4 days *in vitro* (DIV) transfected with GFP alone or together with the indicated PDI constructs. Cells were fixed at 10 DIV and SMI32 staining was performed to identify motoneurons. Images were taken and the total outgrowth of GFP- and SMI32-positive cells was quantified. Results are compiled from three independent experiments.

E Human motoneurons were differentiated from the human embryonic stem cell (ESC) HuESC 3 Hb9::GFP line. Differentiated neurons were transduced with lentivirus expressing GFP alone or together with PDI-expressing plasmids. Transduced cells were cultured for another 10 days. To identify motoneurons after lentiviral transduction, immunocytochemistry analyses were performed. Quantification of neurite outgrowth in the different experimental conditions of GFP- and HB9-positive neurons was obtained. Neurite number and assessment of the length of each neurite were performed in a similar manner as for primary rat motoneurons (see Materials and Methods). Four independent experiments were performed.

F NSC34 cell lines stably knocked down for PDIA1 or ERp57 were differentiated for 24 h in Neurobasal medium containing B27 supplement to induce cell differentiation. The percentage of cells with neurites was quantified in the three independent experiments. A minimum of 100 cells per experiment were analyzed.

Data information: Statistical analyses were performed using one-way ANOVA and Bonferroni's *post hoc* tests. Mean ± SEM with only statistically significant *P*-values are shown: $*P \leq 0.05$; $**P \leq 0.01$; $***P \leq 0.001$. Scale bars represent 25 μm (B, D and E).
Source data are available online for this figure.

and 4A). As controls, we included previously reported substrate-trapping mutants in which one cysteine (Cys) in each active site was exchanged to alanine ($PDIA1^{Cys}$ or $ERp57^{Cys}$) (Jessop *et al*, 2009). These results suggest that mutant PDIs form altered disulfide-dependent complexes with an increased number of substrates or binding partners.

Published online: February 11, 2016
The EMBO Journal

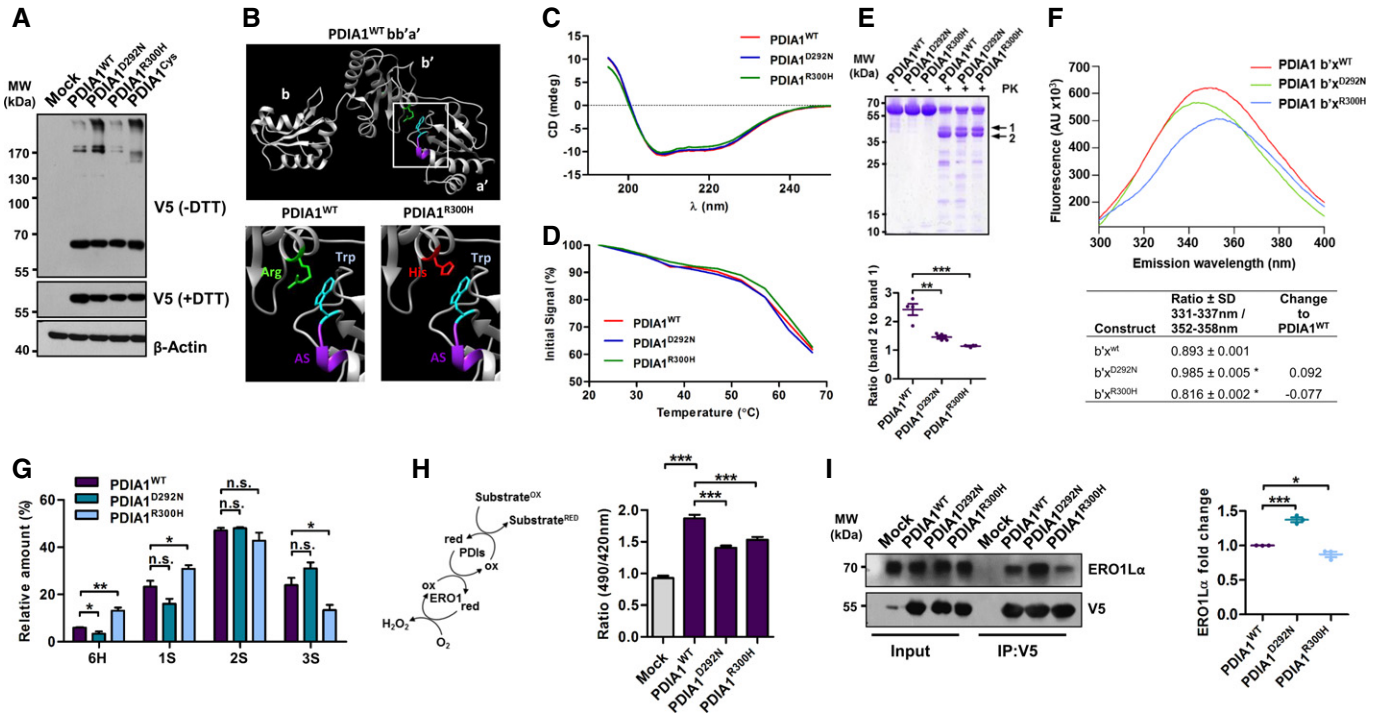

Figure 3. Effects of ALS-linked mutations in PDIA1 on the structure and enzymatic activity.

A PDI mutants form abnormal disulfide-dependent protein complexes. NSC34 cells were transiently transfected with expression vectors for V5-tagged wild-type and mutant PDIA1. After 48 h, differential disulfide-dependent interactions/aggregations of overexpressed PDI variants was assessed under reducing (+DTT) and non-reducing (−DTT) conditions in an 8% SDS–PAGE. Anti-V5 was used for detection in Western blot.

B Analysis of the PDIA1 structure to model the effects of the R300H mutation. The close association between Arg^{300} located to the **b**′ domain of PDIA1 with Trp^{396} located to the **a**′ domain adjacent to the active-site motif CGHC (designated as AS in yellow) is shown in comparison with the mutated version of $PDIA1^{R300H}$ highlighting the same residues. A potential stabilization of the interaction between the **b**′ and **a**′ domain is shown that may be caused by the interaction of the imidazole rings of mutated His^{300} with Trp^{396}.

C ALS-linked PDIA1 variants were generated as recombinant proteins and then analyzed by circular dichroism (CD). Averages for CD spectroscopic scans of $PDIA1^{WT}$ and mutants are shown.

D Averages for CD spectroscopic thermal denaturation of recombinant $PDIA1^{WT}$ and mutants.

E Representative electrophoresis analysis of proteinase K-treated recombinant PDIA1 variants. Mass spectrometric analysis of proteinase K-digested samples from total sample and from in-gel trypsin-digested protein samples (arrows indicate band 1 and band 2) indicated differences in the removal of the x-linker region. Bottom panel: ratios of band 1 to band 2 were quantified in four independent experiments.

F Representative fluorescence spectra of recombinant PDIA1 $b'x^{WT}$ fragments and the equivalent ALS-linked mutants (n = 6). Ratios from the two peak areas and change compared to PDIA1 $b'x^{WT}$. Both mutants analyzed show a significant shift in peak position compared to wild type, but in opposite directions, suggesting that $PDIA1^{D292N}$ shifts equilibrium toward the capped version (x-region over the binding pocket) and the $PDIA1^{R300H}$ mutant toward the uncapped version (Nguyen *et al*, 2008).

G The activity of recombinant PDIA1 was measured *in vitro* using a BPTI refolding assay following by mass spectrometry analysis. The percentages of different BPTI species was calculated (6H, fully reduced; 1S, one disulfide bond; 2S, two disulfide bonds; 3S, three disulfide bonds) at time point 2.5 min in four independent experiments.

H Measurement of H_2O_2 levels at the ER lumen of living cells. Left panel: reduced PDIs can be oxidized by ERO1Lα, which then transfers electrons to molecular oxygen (O_2) to generate hydrogen peroxide as product from PDI activity. Right panel: NSC34 cells were transiently co-transfected with ER luminal HyPer sensor and indicated PDIs. After 48 h, the 490/420 nm fluorescence ratio was recorded for 2 min under basal conditions. Means and SEM derived from all cells per condition (n = 55–74) monitored in four independent experiments are shown.

I HEK293T cells were transfected with expression vectors for V5-tagged wild-type and mutant PDIA1, as well as empty vector. After 48 h, V5-tagged proteins were immunoprecipitated and eluted with V5 peptide. The interaction with endogenous ERO1Lα was analyzed by Western blot. The inputs and elutions are shown as control. Right panel: quantification of the degree of interaction is presented.

Data information: Statistical analyses were performed using Student's t-test in (F, G and I) or one-way ANOVA and Bonferroni's *post hoc* tests in (H). Mean ± SEM with P-values: n.s., $P > 0.05$; $^*P \leq 0.05$; $^{**}P \leq 0.01$; $^{***}P \leq 0.001$.
Source data are available online for this figure.

We previously analyzed the available structure of the PDIA1 **bb**′**a**′ fragment (Wang *et al*, 2012) and concluded that the substitution of Arg^{300} in PDIA1 to histidine may result in a **b**′**a**′ interdomain rearrangement (Gonzalez-Perez *et al*, 2015), which could interfere with the redox-dependent substrate binding of PDIA1 (Fig 3B). This mutation may generate an abnormal interaction between Trp^{396} and the imidazole ring of His^{300}, impacting the accessibility to the substrate binding site as well as the active site (adjacent to Trp^{396}) (Fig 3B). The $PDIA1^{D292N}$ mutation is located in the substrate binding **b**′ domain of PDIA1, and, remarkably, a mutation of this

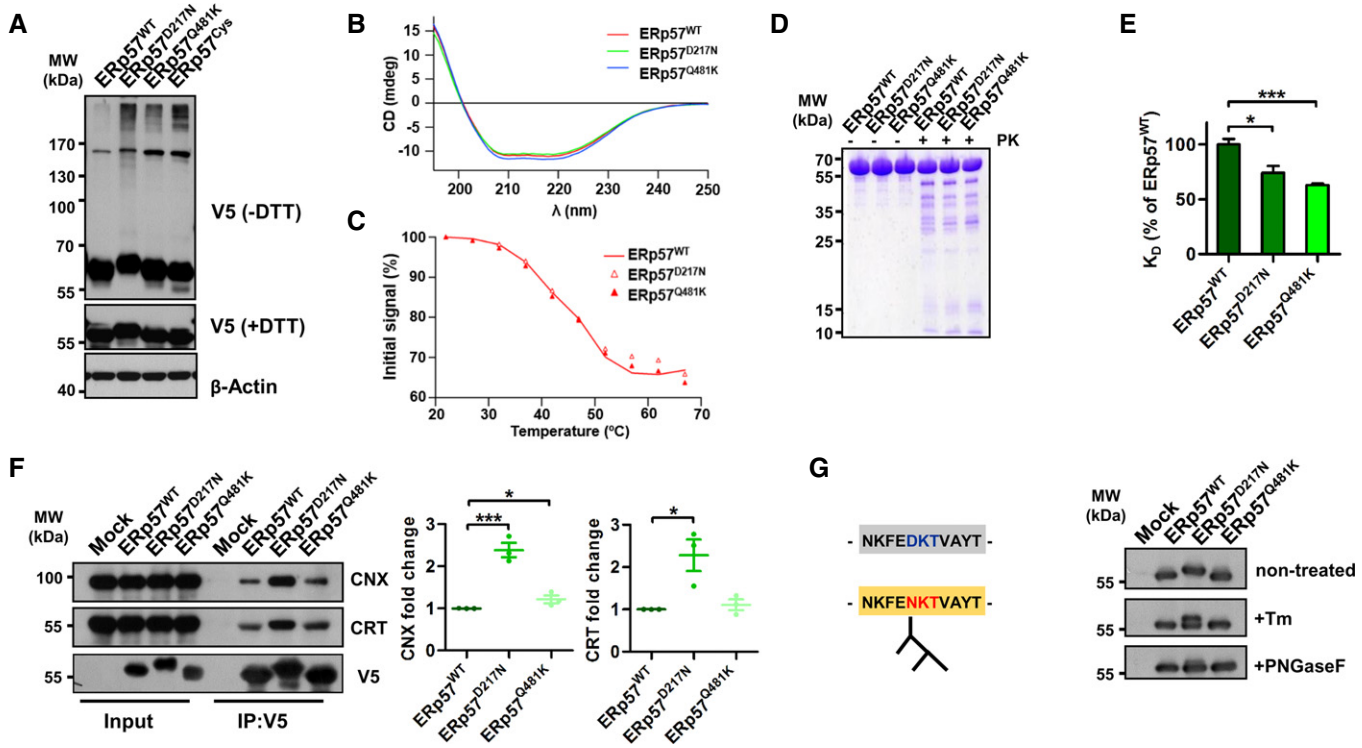

Figure 4. ALS-linked mutations in ERp57 lead to altered interactions with calnexin and calreticulin.

A PDI mutants form abnormal disulfide-dependent protein complexes. NSC34 cells were transiently transfected with expression vectors for V5-tagged wild-type and mutant ERp57. After 48 h, differential disulfide-dependent interactions/aggregations of overexpressed PDI variants was assessed under reducing (+DTT) and non-reducing (−DTT) conditions in an 8% SDS–PAGE. Anti-V5 was used for detection in Western blot.

B ALS-linked ERp57 variants were generated as recombinant proteins and then analyzed by circular dichroism (CD). Averages for CD spectroscopic scans of recombinant $ERp57^{WT}$ and mutants are shown.

C A thermal denaturation curve of $ERp57^{WT}$ and mutants was performed.

D Representative electrophoresis of proteinase K-treated ERp57 recombinant proteins.

E Surface plasmon resonance analysis was performed to monitor the affinity of recombinant ERp57 for recombinant CRT P domain. K_D values are expressed as percentage of $ERp57^{WT}$. Values are derived from four independent experiments. For absolute K_D values, please see Appendix Table S2.

F HEK293T cells were transfected with expression vectors for V5-tagged wild-type and mutant ERp57, as well as empty vector. After 48 h, V5-tagged proteins were immunoprecipitated and eluted with V5 peptide. The interaction with endogenous calnexin (CNX) and calreticulin (CRT) was analyzed by Western blot. The inputs and elutions are shown. Right panel: quantification of the degree of interaction is presented.

G The gain of an N-glycosylation site of $ERp57^{D217N}$ was predicted after the analysis of the protein sequence since the change of Asp^{217} to an Asn creates the NXT/S consensus sequence. Neuro2a cells were transfected with expression vectors for V5-tagged wild-type and mutant ERp57, as well as empty vector and treated with 1 μg/ml tunicamycin (Tm) for 20 h to inhibit N-glycosylation. Alternatively, protein extracts were digested with PNGase F and the possible removal of the N-glycosylation was analyzed by Western blot using anti-V5 antibody.

Data information: Statistical analyses were performed using Student's *t*-test in (E) and (F). Mean ± SEM with *P*-values: $*P \leq 0.05$; $***P \leq 0.001$.
Source data are available online for this figure.

amino acid was already shown to affect the accessibility to the substrate binding site and **a**′ and **b**′ interdomain flexibility (Nguyen *et al*, 2008). To better define possible structural changes in PDIA1 mutants, we generated recombinant proteins for *in vitro* characterization. As determined by far UV circular dichroism, thermal denaturation, and protease resistance assays, we conclude that none of the mutant proteins showed gross structural defects (Fig 3C and D). Minor but significant differences were observed in the proteolytic pattern of the PDIA1 mutants compared with $PDIA1^{WT}$, with both showing altered variation in cleavage around the x-linker region that lies between the **b**′ and **a**′ domains (Fig 3E). In particular, differences were observed in the ratio of the two major degradation products formed (band 1 and 2) (Fig 3E; bottom panel). Mass spectrometry analysis of these bands indicated that PDIA1 mutations resulted in altered variation in cleavage around the **x**-linker region that lies between the **b**′ and **a**′ domains (Fig 3F). The **x**-linker can adopt multiple conformations which determine the accessibility of substrates to the primary substrate binding site in the **b**′ domain (Nguyen *et al*, 2008). Fluorescence analysis of single tryptophan of isolated **b**′**x** constructs showed that $PDIA1^{D292N}$ mutation results in a significant shift in the equilibrium toward the capped state, where the **x**-region blocks access to the binding pocket, while the $PDIA1^{R300H}$ mutation has the opposite effect (Fig 3F).

To determine the consequences of the mutations on the activity of PDIA1, an oxidative refolding assay was performed using the classical substrate bovine pancreatic trypsin inhibitor (BPTI) (Karala *et al*, 2009). $PDIA1^{R300H}$ showed significantly greater amounts of fully reduced BPTI (indicated as 6H) and lower amounts of native

protein, demonstrating a decrease in catalytic activity (Fig 3G). In contrast, the PDIA1^{D292N} showed significantly decreased amounts of fully reduced BPTI (Fig 3G), consistent with our structural analysis. For disulfide bond formation *in vivo*, ER oxidoreductin 1Lα (ERO1Lα) is the main source of oxidizing equivalents for PDIA1 (Appenzeller-Herzog *et al*, 2010). To maintain its oxidized state, ERO1Lα couples disulfide transfer to PDIA1 with the reduction of molecular oxygen, forming hydrogen peroxide (H_2O_2) (Tavender & Bulleid, 2010) (Fig 3H). We measured local H_2O_2 levels with the ER lumen-targeted fluorescent sensor HyPer in living cells (Enyedi *et al*, 2010) and observed that the expression of PDIA1^{WT} led to a significant increase at basal levels, which was significantly reduced when PDIA1^{R300H} or PDIA1^{D292N} were tested (Fig 3H). These effects may reflect altered re-cycling of PDIA1 to its active form. This hypothesis is supported by the occurrence of increased binding of ERO1Lα to PDIA1^{D292N} and decreased binding of ERO1Lα to PDIA1^{R300H} as measured in co-immunoprecipitation experiments of PDIs with endogenous ERO1Lα (Fig 3I). Taken together, our results suggest both PDIA1 mutations may alter the binding-release cycle for substrates.

ALS-associated ERp57 variants display altered interactions with CNX and CRT

As part of the CNX-CRT cycle, ERp57 is responsible for disulfide bond formation of a subset of glycosylated proteins (Maattanen *et al*, 2010). Structural analysis of the available ERp57 structure suggests that the ALS-linked mutation D217N results in a loss of a negative charge in the proximity of a domain containing the positively charged residues K214, R274, and R282 known to facilitate the binding of the negatively charged P domain of CNX or CRT (Pollock *et al*, 2004; Silvennoinen *et al*, 2004; Kozlov *et al*, 2006; Dong *et al*, 2009). The Q481K mutation may also influence the binding to CNX based on its location as previously suggested (Pollock *et al*, 2004). Like PDIA1 mutants, recombinant ERp57 variants did not show any significant alteration in their structure as measured by far UV circular dichroism, thermal denaturation, and protease resistance assays (Fig 4B–D). Based on the predicted physicochemical changes of ERp57 upon mutation, we used surface plasmon resonance analysis to measure the direct binding to the CRT P domain. We observed a significant increase in affinity of both ERp57^{D217N} and ERp57^{Q481K} for the P domain of CRT (Fig 4E and Appendix Table S2). To confirm these findings in living cells, we performed immunoprecipitation experiments using HEK293T cells. We found that ERp57^{D217N} displays a strong increase in the binding to endogenous CRT and CNX, whereas ERp57^{Q481K} displayed only a slight increase in the binding to both lectins (Fig 4F).

Of note, we also observed a shift in the electrophoretic pattern of ERp57^{D217N} when expressed in zebrafish, as well as in NSC34 cells, but not with the recombinant protein. Analysis of the sequence surrounding this mutation site revealed that the change of Asp^{217} to Asn creates a putative artificial N-linked glycosylation site (NKT), a phenomenon previously described for pathogenic gene variants in other diseases (Vogt *et al*, 2007). Consistent with this prediction, treatment of cells with tunicamycin, an inhibitor of N-glycosylation, reversed the electrophoretic shift observed upon ERp57^{D217N} expression (Fig 4G). Similar results were observed by digesting cell extracts with PNGase F to remove N-linked glycosylations (Fig 4G). Together, these biochemical studies identified distinct structural and functional defects of these ALS-linked PDI mutants, which are likely to impact the function of these foldases.

Deletion of ERp57 in the CNS results in impaired motor performance

The function of PDIs in the physiology of the nervous system remains largely unexplored. Since ALS patients presented mutations in *PDI* genes in one allele and our *in vitro* studies suggest a loss of function according to our differentiation assays, we determined whether *PDI* haploinsufficiency could have an impact in the motor function of the nervous system. Therefore, we generated a conditional knockout mouse for *ERp57* using the *lox*P and Cre recombinase system under the control of the neuronal progenitor promoter Nestin (referred to as ERp57$^{Nes-/-}$ mice). We were able to obtain viable animals, indicating that ERp57 deficiency in the brain bypassed the embryonic lethality observed in full knockout animals. Analysis of ERp57 expression levels in spinal cord tissue and brain indicated a complete deletion of ERp57, whereas heterozygous animals (ERp57$^{Nes+/-}$) presented a 50% reduction in the protein levels (Fig 5A). Targeting *ERp57* in the nervous system led to a retardation of growth as measured by the progression of body weight gain (Fig 5B). In addition, a substantial reduction in the rate of ERp57$^{Nes-/-}$ animals born was detected, as compared to the expected Mendelian proportions (Table 1).

We then analyzed several behavioral parameters normally affected in ALS models to measure coordination and the motor activity. Remarkably, ERp57 haploinsufficiency (ERp57$^{Nes+/-}$) led to a significant decline in rotarod performance compared to littermate ERp57^{WT} mice, which was further exacerbated in ERp57$^{Nes-/-}$ animals (Fig 5C). This effect was stable over time (Appendix Fig S3A). Analysis of motor strength and coordination using the hanging test also revealed clear deficits in *ERp57* knockout mice and intermediate phenotypes in heterozygous animals (Fig 5D and Videos EV1, EV2 and EV3). Unexpectedly, a subgroup of ERp57$^{Nes-/-}$ animals died prematurely; where nine out of 19 animals died before 150 days of age (Fig 5E). Thus, loss of ERp57 function in the central nervous system results in motor dysfunction and premature death, suggesting a functional role of this PDI in neurons.

We then performed histological analysis of spinal cord tissue of ERp57$^{Nes-/-}$ mice. Immunofluorescence analysis of the distribution of neurons in the spinal cords of the ERp57$^{Nes+/-}$ and ERp57$^{Nes-/-}$ mice revealed no obvious changes in the ventral horn neuron densities after NeuN staining (Fig 5F). These results were confirmed by quantitative stereological analysis of spinal cord tissue after Nissl or choline acetyltransferase (ChAT) staining (Fig 5G). In addition, no signs of astrogliosis were detected in the spinal cord of ERp57$^{Nes-/-}$ mice using GFAP staining (Fig 5F). Similarly, visualization of Purkinje cell distribution in the cerebellum indicated normal neuronal counts (Appendix Fig S3B). In contrast to the phenotype described to CNX knockout animals (Kraus *et al*, 2010), no changes in spinal cord myelination were found in ERp57$^{Nes-/-}$ animals (Fig 5H). Thus, ERp57 deficiency results in motor problems in the absence of evident signs of motoneuron cell death, suggesting the occurrence of altered neuronal dysfunction rather than a neurotoxic effect.

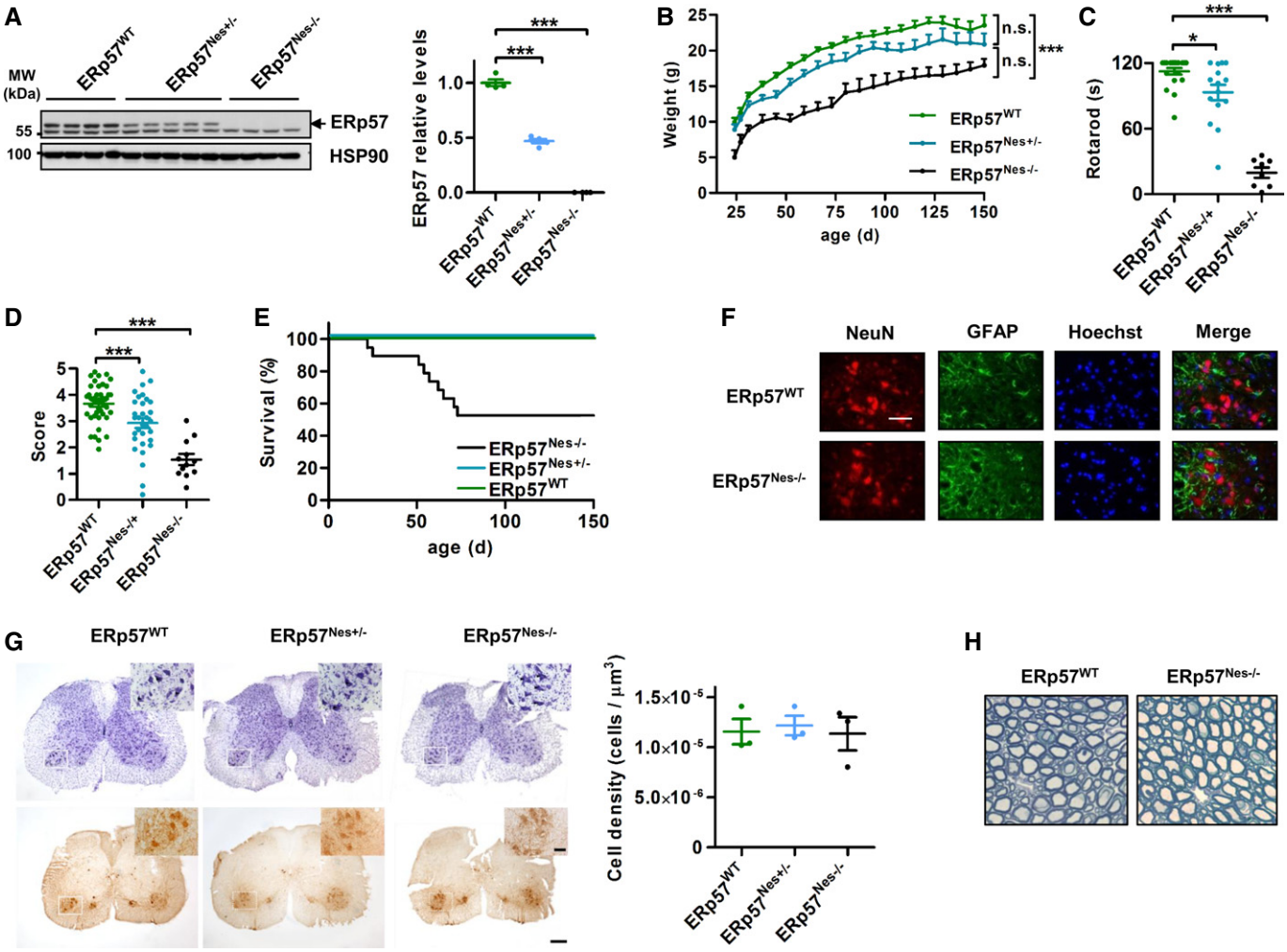

Figure 5. ERp57 deficiency in the nervous system leads to motor dysfunction and premature death.

A ERp57$^{flox/flox}$ mice were crossed with Nestin-Cre transgenic mice to generate nervous system-specific ERp57-deficient animals. The levels of ERp57 protein in the spinal cord were monitored by Western blot. ERp57^{WT}: n = 4, ERp57$^{Nes+/-}$: n = 5, and ERp57$^{Nes-/-}$: n = 4 mice. HSP90 levels were used as a loading control. Right panel: quantification of ERp57 levels was performed relative to Hsp90 levels.

B Body weight measurements were performed at the indicated time points in ERp57^{WT} (n = 50), ERp57$^{Nes+/-}$ (n = 32) and ERp57$^{Nes-/-}$ (n = 19) mice.

C Rotarod performance was performed ERp57^{WT} (n = 20), ERp57$^{Nes+/-}$ (n = 15) and ERp57$^{Nes-/-}$ (n = 8) mice.

D Hanging test performance was assessed in ERp57^{WT} (n = 41), ERp57$^{Nes+/-}$ (n = 32), and ERp57$^{Nes-/-}$ (n = 12) mice.

E Kaplan–Meier survival curve for ERp57$^{Nes-/-}$ mice (N = 19) that prematurely died or had to be sacrificed because of health reasons between the ages 22 and 73 days. Mean survival of this subgroup of animals was 57 days. ERp57^{WT} (n = 50) and ERp57$^{Nes+/-}$ (n = 32) mice are shown as a reference.

F Histological analysis of NeuN and GFAP staining was performed in spinal cord tissue from ERp57^{WT} and ERp57$^{Nes-/-}$ mice in three animals per group using indirect immunofluorescence. The nucleus was stained with Hoechst. Representative images from one mouse per group are shown. Scale bar: 50 µm.

G Stereological analysis of the spinal cord from ERp57^{WT} (n = 4), ERp57$^{Nes+/-}$ (n = 4) and ERp57$^{Nes-/-}$ (n = 4) mice. Alternate series of sections from the spinal cord of the mice were either stained for Nissl (top row images) or processed for immunohistochemistry for the cholinergic cell marker choline acetyltransferase (ChAT, bottom row images). The nucleoli of the motoneurons, as stained in the Nissl series, were counted inside the motoneurons pools previously defined using the adjacent ChAT series (contours not shown). Cell densities of the three genotypes are shown on the right plots. No significant differences were found between the genotypes. Scale bar represents 200 µm and 50 µm on large and inset images, respectively.

H Representative images of the spinal cord myelination of ERp57^{WT} and ERp57$^{Nes-/-}$ mice.

Data information: For statistical analysis, two-way ANOVA with Bonferroni's *post hoc* test was performed in (B) and one-way ANOVA with Bonferroni's *post hoc* test was performed in (A, C and D). Mean ± SEM with P-values: n.s., non-significant, $P > 0.05$; *$P \leq 0.05$; ***$P \leq 0.001$.
Source data are available online for this figure.

ERp57 deficiency causes neuromuscular defects

Our studies in zebrafish suggested that PDI mutants have adverse effect on neuromuscular connectivity but not on overall motoneuron survival. To assess the impact of ERp57 deficiency on motoneuron function *in vivo*, we performed electromyography (EMG) measurements. Fifty percent of ERp57$^{Nes+/-}$ and all ERp57$^{Nes-/-}$ mice tested displayed fibrillations and positive sharp

Published online: February 11, 2016
The EMBO Journal

Table 1. Generation rate of ERp57 wild-type, heterozygous, and conditional knockout of indicated mouse crossings.

Crossings	Pups			Total
	$ERp57^{WT}$	$ERp57^{Nes+/-}$	$ERp57^{Nes-/-}$	
$ERp57^{WT/flox}$ × $ERp57^{WT/flox}$ – Cre Tg				
Observed No.	134	24	8	166
Observed %	80.7	14.5	4.8	100
Expected %	62.5	25	12.5	100
$ERp57^{flox/flox}$ × $ERp57^{WT/flox}$ – Cre Tg				
Observed No.	82	27	13	122
Observed %	67.2	22.1	10.7	100
Expected %	50	25	25	100

waves (Fig 6A), suggesting a loss of integrity of NMJs. As a positive control for this test, a symptomatic $SOD1^{G86R}$ transgenic mouse was monitored (Appendix Table S3). The loss of neuromuscular synapses is one of the first signs of ALS, leading to progressive loss of motor control. Based on the functional impairment to the motor capacities of ERp57 mice, we extensively analyzed NMJs in the diaphragm, one the relevant muscles that loses the innervation in ALS (Dupuis *et al*, 2009; Perez-Garcia & Burden, 2012; Liu *et al*, 2013). The analysis of NMJ distribution in ERp57-deficient mice revealed a narrower band of acetylcholine receptor (AChR) clusters along the length of the diaphragm compared to wild-type control animals (Fig 6B, upper panel). Quantification of the number of bins revealed a significant reduction in $ERp57^{Nes-/-}$ animals (Fig 6B, bottom panel). Three-dimensional reconstructions of NMJs indicated that ERp57 deficiency resulted in abnormal postsynaptic morphologies and reduced muscle innervation (Fig 6C). Remarkably, ERp57-deficient animals displayed either incomplete or aberrantly distributed NMJs, while the number of fully innervated normal pretzel-like NMJs was strongly diminished (Fig 6C and D, and Videos EV4–EV7). Detailed quantitative analyses of postsynaptic NMJ morphologies indicated a significant increase of altered NMJs in $ERp57^{Nes+/-}$ and $ERp57^{Nes-/-}$ diaphragms, we observed a clear accumulation of dismantled NMJs in both genotypes (Fig 6D). Consistent with these results, quantifications of the area and perimeter of NMJs indicated a significant reduction of both parameters in $ERp57^{Nes+/-}$ and $ERp57^{Nes-/-}$ animals (Fig 6E). These

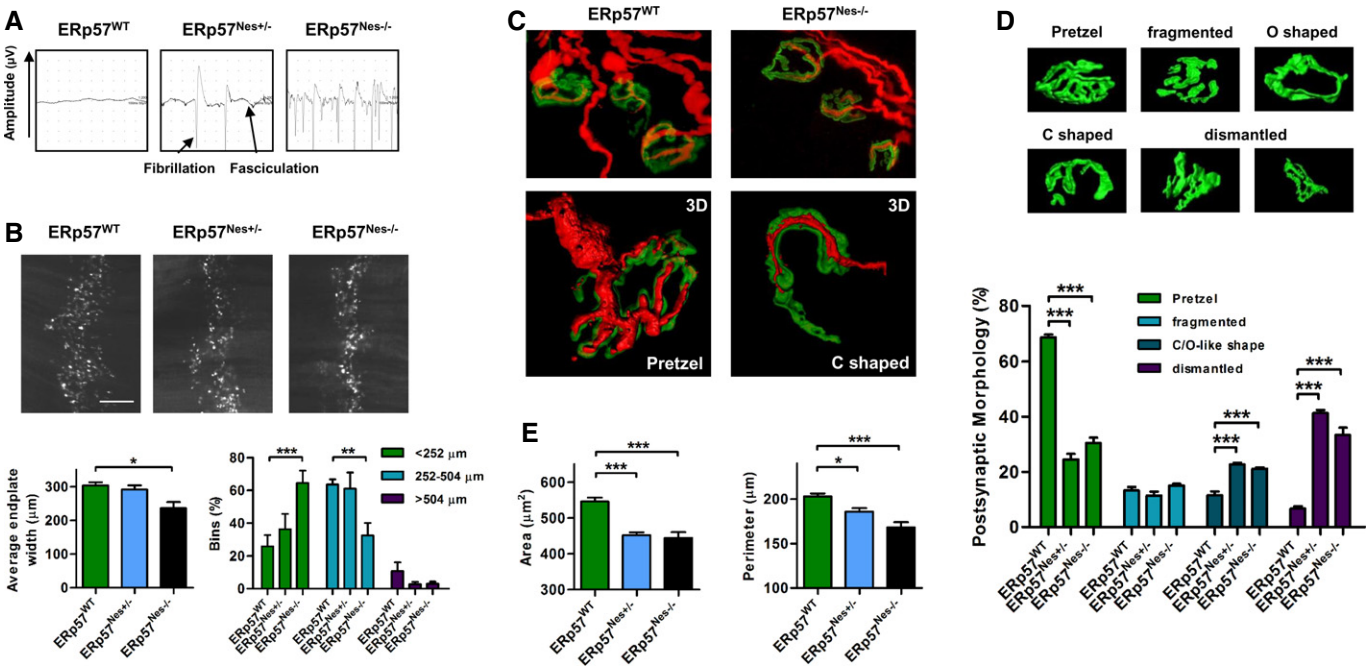

Figure 6. ERp57 deficiency results in loss of neuromuscular connectivity.

A Representative EMG recordings of $ERp57^{WT}$ (n = 16), $ERp57^{Nes-/+}$ (n = 12) and $ERp57^{Nes-/-}$ (n = 5) mice is presented. The presence of positive sharp waves (PSW) in $ERp57^{Nes+/-}$ and $ERp57^{Nes-/-}$ mice indicated muscle denervation.

B Analysis of NMJ and muscle morphologies were performed in $ERp57^{WT}$ (n = 5), $ERp57^{Nes+/-}$ (n = 5) and $ERp57^{Nes-/-}$ (n = 4) mice. Quantifications of endplate width, measuring the most ventral region of the diaphragms every 134 µm considering both sides of the innervation profile. Twenty to forty measurements per diaphragm were obtained per animal.

C Whole-mounted diaphragms from $ERp57^{WT}$ and $ERp57^{Nes-/-}$ mice were co-stained with anti-neurofilament (red) and α-BTX to reveal the postsynaptic densities (green). Three-dimensional reconstructions (lower panel) of higher magnification are shown. $ERp57^{WT}$ NMJs are fully innervated pretzel-like, whereas $ERp57^{Nes-/-}$ NMJs display less complex postsynaptic densities and an incomplete or aberrantly distributed innervation pattern (Videos EV4–EV7).

D Representative 3D reconstructions of z-stacks showing the five categories in which NMJ morphologies were grouped: pretzel, fragmented, O-shaped, C-shaped, and dismantled NMJs. Histogram of the distribution frequency of > 200 different NMJ per animal is shown.

E Quantitative morphometry of > 60 NMJs in the different genotypes analyzed.

Data information: For statistical analysis, one-way ANOVA with Bonferroni's *post hoc* test was performed in (B, D, and E). Mean ± SEM with P-values: *$P \leq 0.05$; **$P \leq 0.01$; ***$P \leq 0.001$.

results indicate that the motor defects observed in ERp57 conditional knockout mice are associated with a drastic perturbation of neuromuscular connectivity.

Based on the altered NMJs in ERp57-deficient mice, we then analyzed the possible consequences in muscle physiology. We confirmed that the expression levels of ERp57 in the muscle of ERp57$^{Nes-/-}$ mice were not affected (Fig 7A). By assessing the overall integrity of the muscle, no gross changes were found in muscle morphology (Fig 7B, top panel), skeletal muscle fibrosis (Fig 7B, middle panel), or degeneration/regeneration cycles (Fig 7B, lower panel). Since the functional and structural properties of skeletal muscle depend on motor axon innervation, we assessed muscle morphology in *Tibialis anterior* sections stained for NADH-TR activity to identify oxidative myofibers (Fig 7B). NADH-TR positive (slow twitch) and negative (fast twitch) myofibers were quantified as percentage of total for each genotype. This analysis revealed an altered distribution of oxidative myofibers in ERp57-deficient animals (Fig 7C). Furthermore, the mean diameter of slow- and fast-twitch muscle fibers was reduced in ERp57$^{Nes-/-}$ animals (Fig 7C). In summary, these results indicate that ERp57 deficiency in the nervous system leads to a profound impairment of motor control, possibly caused by disrupting neuromuscular synapses, and as a consequence, altered muscle physiology. The global phenotype of ERp57$^{Nes-/-}$ animals may resemble an early symptomatic stage of ALS and other neuromuscular disorders.

Targeting ERp57 in the nervous system alters the expression of SV2 synaptic protein

Sporadic ALS cases are associated with the accumulation of abnormal protein aggregates containing proteins that are also mutated in a small percentage of familial cases including TDP43 and SOD1 (Turner *et al*, 2013). To assess whether the loss of ERp57 has any consequences on wild-type SOD1 and TDP43, we monitored their expression levels and aggregation status in the brain cortex of ERp57-deficient animals. We did not observe any clear aggregation

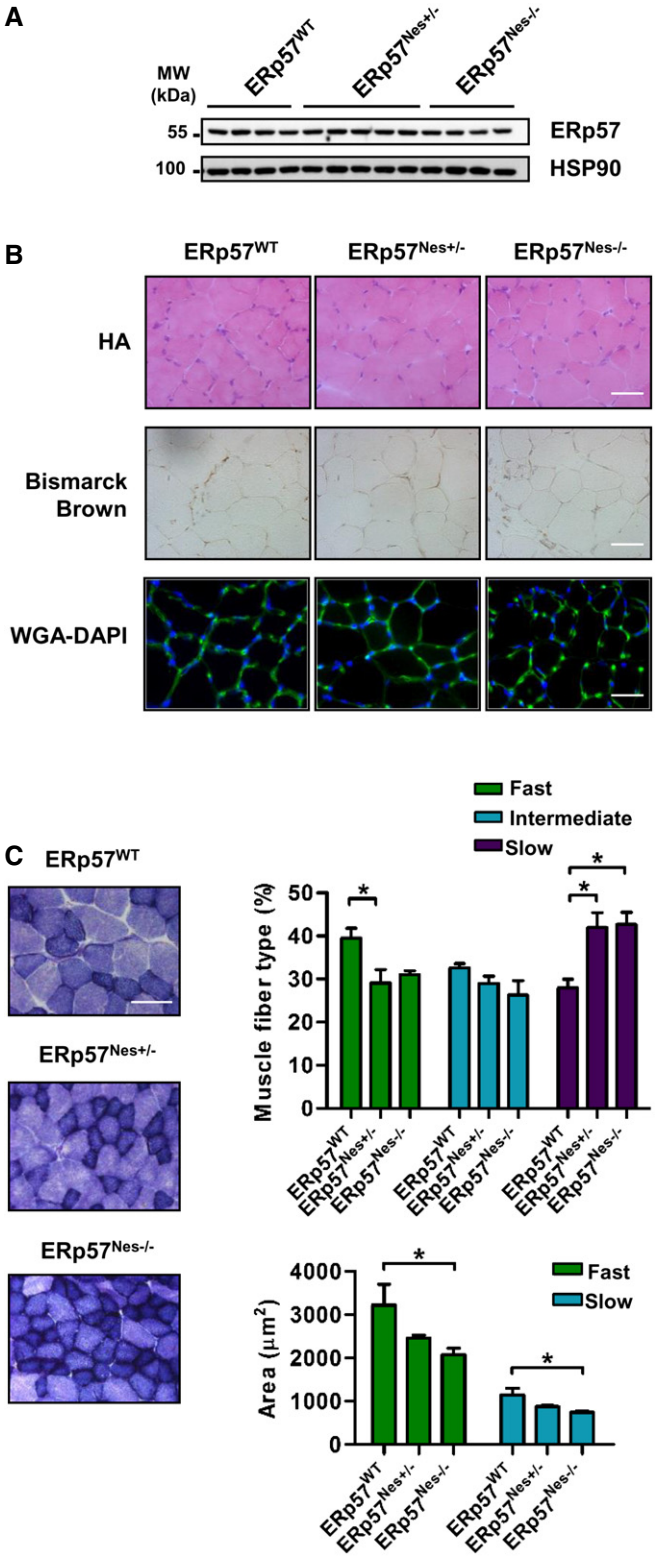

Figure 7. ERp57-deficient mice display aberrant skeletal muscle fibers.

A The levels of ERp57 protein in the muscle were monitored by Western blot. ERp57^{WT} (n = 4), ERp57$^{Nes+/-}$ (n = 5), and ERp57$^{Nes-/-}$ (n = 4) mice. HSP90 was used as a loading control.

B Tibialis anterior muscles from ERp57^{WT} (n = 5), ERp57$^{Nes+/-}$ (n = 5), and ERp57$^{Nes-/-}$ (n = 4) mice were dissected and cryosectioned (20 μm) for the analysis of several parameters of muscle physiology. Upper panel: hematoxylin/chromotrope (HA) staining was performed to assess the gross morphology of the muscle. Middle panel: Bismarck brown staining to monitor skeletal muscles fibrosis. Lower panel: cryosections were then double stained with wheat germ agglutinin (WGA) to visualize plasma membrane and nuclei. The absence of central nuclei in all genotypes suggests that ERp57 deficiency does not affect degeneration/regeneration cycles. Images are representative of each genotype and where acquired in the same anatomical region of the TA muscles.

C Tibialis anterior cryosections (20 μm) from ERp57^{WT}, ERp57$^{Nes+/-}$, and ERp57$^{Nes-/-}$ mice were stained for NADH-TR activity to identify oxidative myofibers (left panel). Representative micrographs of transversal cryosections show variable proportions of light, intermediate and dark positive staining in the different genotypes: NADH-TR-positive (slow twitch) and NADH-TR-negative (fast twitch) myofibers were quantified as percentage of total for every genotype (upper right panel). The mean diameter of slow- and fast-twitch muscle fibers was evaluated at the light microscope using the ImageJ software (lower right panel). Data represent the average ± SEM of > 300 fibers per animal.

Data information: Scale bars represent 50 μm (B, C). For statistical analysis one-way ANOVA with Bonferroni's *post hoc* test was performed in (C). Mean ± SEM with P-values: *$P \leq 0.05$.
Source data are available online for this figure.

of these proteins using Western blot analysis or a filter trap assay (Appendix Fig S4A–D). As positive controls, protein extracts from mutant SOD1^{G86R} or TDP43^{A315T} transgenic mice were used to visualize protein aggregates. Similarly, no changes in SOD1 or TDP43 levels were observed in the spinal cord of these animals (Appendix Fig S4E).

Overall our results suggest that ERp57 deficiency in the nervous system triggers motor defects associated with alterations to the neuromuscular junctions, indicating detrimental consequences at the functional level rather than a neurotoxic mechanism. Synaptic proteins and receptors are generally folded at the ER and traffic through the secretory pathway to reach their final destination. Many of them are disulfide bonded, glycosylated, or both and therefore represent potential substrates of ERp57. We analyzed the expression of a panel of synapse-located proteins in the brain cortex of ERp57-deficient animals including synaptic vesicle protein SV2, the presynaptic marker synaptophysin, and postsynaptic marker PSD95, as well as NMDA receptor 2A (NMDAR2A). Remarkably, from this screening, a significant decrease in the levels of SV2 was observed in both ERp57$^{Nes+/-}$ and ERp57$^{Nes-/-}$ animals (Fig 8A and B). In addition, we observed the accumulation of high molecular weight species of SV2 (Fig 8A and B), suggesting the occurrence of abnormal aggregation similar to the phenotype observed for well-characterized ERp57 substrates (Jessop *et al*, 2009). These alterations were not evident in the spinal cord of ERp57-deficient animals, possibly because the expression levels and isoforms detected in this tissue were lower than in brain cortex (Appendix Fig S5). These results indicate that ERp57 alters the expression of SV2, an essential protein mediating synapse function in the nervous system.

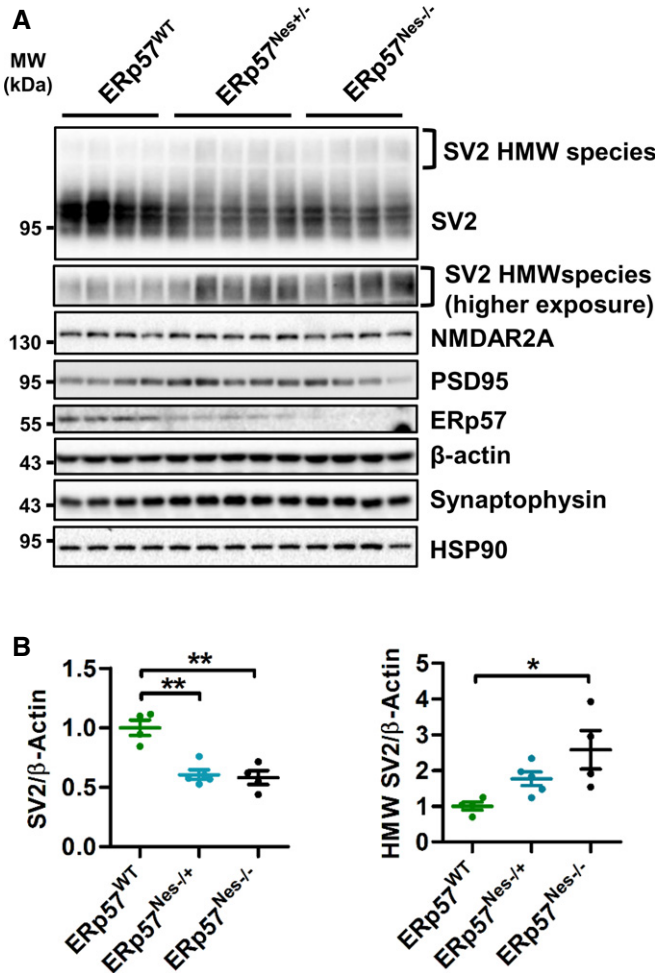

Figure 8. Loss of ERp57 in the cortex results in lower levels of the synaptic protein SV2.

A The levels of synaptic proteins SV2, NMDAR2A, PSD95, and synaptophysin in the cortex were monitored by Western blot. ERp57^{WT} (n = 4), ERp57$^{Nes+/-}$ (n = 5) and ERp57$^{Nes-/-}$ (n = 4) mice. HSP90 and β-actin were used as loading controls.

B Quantification of SV2 monomer (left panel) and SV2 high molecular weight species (right panel). β-actin was used as the reference.

Data information: For statistical analysis one-way ANOVA with Bonferroni's post hoc test was performed in (B). Mean ± SEM with P-values: *$P \leq 0.05$, **$P \leq 0.01$.

Source data are available online for this figure.

Discussion

The upregulation in the levels of PDI family members is a salient feature of ALS, as well as other neurodegenerative diseases including Alzheimer's, Parkinson's, and Creutzfeldt-Jacob disease (reviewed in Andreu *et al*, 2012). Therefore, PDI family members are emerging as relevant stress-response genes in diverse neurological disorders; however, little is known about how PDIs contribute to these pathologies. Since PDIs participate in many processes including protein folding, ER-associated degradation (ERAD), protein quality control, redox homeostasis, cell signaling, and apoptosis (Grek & Townsend, 2014), disruption of their function may affect hundreds of substrates. Here, we have uncovered an unanticipated function of PDIs in motor control and neuromuscular connectivity. Using a series of complementary approaches, we describe a novel pathological mechanism of ALS where PDI malfunction appears to correlate with a striking alteration in the morphology of NMJs, possibly contributing to the abnormal motor control observed in ERp57 conditional knockout mice. Our findings are in agreement with recent studies in prion and Alzheimer's disease models suggesting that chronic disturbances to ER function could trigger a reduced synthesis of synaptic proteins, leading to cognitive and motor impairment rather than neuronal loss (Moreno *et al*, 2012; Ma *et al*, 2013). We speculate that perturbations to the PDI folding network operate as a probable ALS risk factor, consistent with the view that altered ER proteostasis can drive neuronal dysfunction and degeneration during the disease (Roussel *et al*, 2013; Hetz & Mollereau, 2014).

For several reasons, it is likely that the ALS-linked PDI variants studied here trigger neuronal dysfunction through a subtle progressive adverse impact on motoneuron function. First, to differing degrees, the PDI variants reported here induced motoneuron pathology in zebrafish, analogous to that induced by mutant SOD1, FUS, TDP43, and *C9orf72* in this vertebrate model (Kabashi *et al*, 2009, 2011; Armstrong & Drapeau, 2013; Lee *et al*, 2013; Babin *et al*, 2014). Second, the four PDI variants analyzed were clearly adverse for motoneurons *in vitro*, disturbing dendritic elongation and morphology, which may affect neuronal connectivity,

although they were not overtly neurotoxic to the cultured motoneurons. This is in agreement with recent studies of iPSC-derived ALS motoneurons expressing different genetic mutations in which morphological alterations, rather than neurotoxicity, are a major and consistent phenotype (Chen *et al*, 2014; Kiskinis *et al*, 2014). Importantly, we provide evidence indicating that the expression of wild-type PDIA1 and ERp57 contribute to the process of neuronal outgrowth. We speculate that PDIs regulate to some degree the composition and structure of synapses through their folding and quality control function at the ER. Additionally, other mechanisms may be relevant including the modulation of cytoskeleton dynamics, since ERp57 has a relevant activity on regulating ER calcium release (Li & Camacho, 2004). Furthermore, our results are reminiscent of findings with mutant SOD1 transgenes, which in many neuronal culture systems do not elicit a lethal phenotype, yet impair neuronal functionality. Third, loss of ERp57 in mice triggers motor dysfunction without motor neuron loss, possibly by altering neuromuscular synapses. While the mechanism for this striking phenotype remains unclear, our data suggest that altered morphology of the NMJ may contribute to the motor dysfunction. We are currently performing proteomic studies to identify PDI substrates altered after expression of ALS-linked PDI variants. We speculate that functional disturbances of PDIs may be involved in the initial stages of ALS where neuromuscular alterations rather than motoneuron loss (a late event in the disease and most models) drive the appearance of disease signs. Importantly, ER proteostasis impairment is the earliest defects observed in SOD1 mutant mice before denervation occurs (Saxena *et al*, 2009) and recent studies have associated these alterations to the abnormal hyperexcitability observed in ALS motoneurons (Kiskinis *et al*, 2014). Besides, changes in neuronal functionality observed here may also relate to the non-motor symptoms observed in a subgroup of ALS patients (Ling *et al*, 2013). Fourth, the variants were all heterozygous missense changes, arguing either that they exert a dominant influence or that the mutant PDI proteins lead to haploinsufficiency, consistent with our functional studies in *ERp57* conditional knockout mice and cell culture models. Homozygosis may also result in early embryonic lethality as observed in *Erp57* knockout animals (Garbi *et al*, 2006). Based on genetic analyses to date, and our biological studies, we consider these PDI mutants as risk factors or modifiers of phenotype rather than causal variants; they may contribute to disease by both gain- and loss-of-function mechanisms.

A few knockout mouse models for PDIs have been described to date, including ERp57, ERp29, ERdj5, PDIA1, and AGR2 (Garbi *et al*, 2006; Park *et al*, 2009; Hosoda *et al*, 2010; Nemere *et al*, 2010; Hahm *et al*, 2013; Hirsch *et al*, 2014). Nevertheless, in none of these studies, CNS-related phenotypes were reported so far when the expression of PDIs was targeted *in vivo*. Recently, however, we reported the generation of the transgenic mouse model overexpressing ERp57 in the CNS. We found that while the overexpression of ERp57 has no effect on the survival of dopaminergic neurons, it enhances peripheral nerve regeneration suggesting a differential role in neuronal vulnerability (Castillo *et al*, 2015). In agreement with the current study, recent findings suggest that motoneurons are selectively vulnerable to perturbations of ER function. A recent study indicates that the differential expression of the BiP cofactor SIL1 underlies the differential vulnerability of the affected motoneuron population in ALS (Filezac de L'Etang *et al*, 2015). Loss of one copy of *SIL1* accelerated experimental ALS enhancing ER stress, whereas its overexpression provided robust neuroprotection (Filezac de L'Etang *et al*, 2015). Furthermore, mutations in *SIL1* result in spontaneous degeneration in mice (Zhao *et al*, 2005) and cause Marinesco-Sjögren syndrome. Interestingly, deletion of one CRT allele in the context of mutant SOD1 transgenic mice led to exacerbated muscle weakness and denervation, accelerating the progression of the disease (Bernard-Marissal *et al*, 2014). Consistent with our results, motoneuron dysfunction in this model did not involve increased motoneuron loss, suggesting also a role of CRT in early ALS phases involving muscle denervation (Bernard-Marissal *et al*, 2015). On the other hand, CNX deficiency leads to motor defects due to alterations in the structure of myelin sheets in the spinal cord (Kraus *et al*, 2010). Finally heterozygous mutation in *BiP* in mice leads to the development of serious motor problems during aging, associated with the selective degeneration of motoneurons and proteostasis alterations including the spontaneous accumulation of SOD1 aggregates (Jin *et al*, 2014). Together with our findings, these data suggest that the perturbations to the ER proteostasis network may contribute to early events in ALS associated with impaired neuromuscular function. Since the capacity of the ER to buffer fluctuations of proteostasis decline with age (Douglas & Dillin, 2010; Mardones *et al*, 2015), it may be feasible that PDI variants have more drastic effects in neuronal connectivity during aging and, together with other ALS risk factors, may translate into an irreversible damage to motoneuron function and the manifestation of the disease. As noted above, we have identified two fundamental consequences of the mutations in PDIA1 and ERp57: (i) a disturbance of the primary foldase function, as indicated by our biochemical and cellular characterization, and (ii) structural and functional changes to the neuromuscular synapse. The alterations in the levels and aggregation state of the synaptic protein SV2 in the brain cortex of ERp57 knockout animals lead us to speculate that persistent subtle changes in synaptic proteostasis may cause in the long term a progressive disturbance of neuronal connectivity. In agreement with this hypothesis, we previously observed a reduction of the steady-state levels of the prion protein (PrP) in the brain of ERp57 knockout mice (Torres *et al*, 2015). Although only a minority of ALS cases are genetically associated with PDI variants, we would argue based on studies depicting altered PDI expression in sALS (Matus *et al*, 2013b) that dysfunction of the PDI foldase network is a relevant factor in ALS. Interestingly, the mutations studied here in PDIs do not cause ER stress and do not affect SOD1 or TDP43 aggregation, suggesting that we uncovered a novel mechanism of ALS pathogenesis. Thus, our findings provide a proof of concept for one possible mechanism underlying the etiology of ALS involving alterations to the ER proteostasis machinery. Hence, PDIs are novel elements in ALS pathogenesis that may ultimately represent an important pathway for future therapeutic intervention.

Materials and Methods

Cell media and antibiotics were obtained from Life Technologies (Maryland, USA). Fetal calf serum was obtained from Atlanta Biologicals. Hoechst was purchased from Molecular Probes. All

transfections were performed using the Effectene reagent (Qiagen). PNGase F was obtained from New England Biolabs; tunicamycin and thapsigargin were obtained from Sigma. DNA was purified with Qiagen kits.

DNA constructs

The pcDNA3.1/V5 plasmids carrying genes for $PDIA1^{WT}$, $PDIA1^{Cys}$, $ERp57^{WT}$, and $ERp57^{Cys}$ were described before (Jessop *et al*, 2007, 2009). Site-directed mutagenesis following manufacturer's instructions was performed to create ALS mutant constructs (Stratagene cat. No. 200517-5). All mutated constructs were verified by DNA sequencing. The plasmid for $HyPerER_{lum}$ was previously described (Enyedi *et al*, 2010). Mature PDIA1 and ERp57, PDIA1 b′x and calreticulin P domain (residues 206–305) constructs were previously cloned into a pET23-based expression vector, which incorporates an N-terminal His-tag to the cloned gene. Site-directed mutagenesis was performed according to instructions of the Pfu™ Turbo DNA polymerase kit (Stratagene, La Jolla, CA, USA), and the resulting constructs were checked by DNA sequencing.

Cell culture assays

NSC34 cells were grown in Dulbecco's modified Eagle's medium–high glucose (DMEM; Gibco), supplemented with 10% fetal bovine serum (FBS), 100 units/ml penicillin, and 0.1 mg/ml streptomycin (Invitrogen) at 37°C under 5% CO_2. Routinely, cells were transfected with Effectene transfection reagent (Qiagen) using the recommended protocol by the manufacturer.

We generated stable motoneuron cell lines (NSC34) with reduced levels of PDIA1 and ERp57 by targeting the respective mRNA with shRNA as reported before (Lisbona *et al*, 2009). Targeting sequences for the mouse *Pdia1* and *Erp57* mRNA are 5′-CCCAA GAGTGTATCTGACTAT-3′ and 5′-GACCAGTTTATGTTTGTGGTT, respectively. The efficiency of the knockdown was analyzed by conventional PCR, using the primers 5′-CAAGATCAAGCCCCACC TGAT-3′ (F) and 5′-AGTTCGCCCCAACCAGTACTT-3′ (R) (83 pb amplicon) for PDIA1 and 5′-GTCATAGCCAAGATGGATGCC-3′ (F) and 5′-TTAATTCACGGCCACCTTCATA-3′ (R) (133 amplicon) for ERp57.

For differentiation assays, NSC34 cells were transiently co-transfected with pEGFP-N1 and pcDNA3.1/V5 coding for PDIA1 or ERp57 constructs. Alternatively stable cell lines knocked down for PDIA1 or ERp57 were used. Cells were split 20 h post-transfection. About 50,000 cells were re-seeded in a 6-well format in DMEM medium with 1% FBS. After 4 h attachment of cells to the plate was completed, at which time they were washed once with 1 ml PBS pH 7.4, and the medium was changed to Neurobasal with 2% B27 supplement, 2 mM glutamine, and 2× Pen/Strep. Following 24 h of incubation, a minimum of 6 pictures were taken per condition per experiment using an Olympus IX71 microscope. Neuronal outgrowth was determined by analyzing the percentage of cells with neurites and the average length of neurites per condition using the Metamorph software (Universal Imaging, USA). A minimum of 100 cells per experiment were analyzed.

For cell viability assays, 50,000 cells per well were seeded in 12-well plates and the maintained for 24 h. Cells were then transiently transfected with PDIA1 or ERp57 constructs. Cell viability was monitored using PI staining. Toxicity of ER stressors thapsigargin (concentrations 20, 100, and 500 nM) or tunicamycin (1 μg/ml) was analyzed by MTT assay (Promega). Immunofluorescence was performed using standard methods followed by Manders coefficient calculations (Ramirez *et al*, 2009). Local ER H_2O_2 levels were assessed in NSC34 cells co-transfected with pcDNA3.1/V5 plasmids carrying PDIA1 and ERp57 constructs and the $HyPerER_{lum}$ plasmid, similar as we recently described (Matus *et al*, 2013a). Secretion of progranulin was measured in cell culture medium using an ELISA kit (Alexis Biochemicals, San Diego, CA) according to the manufacturer's instructions.

Morphological analysis of motoneurons

Ventral spinal cord neurons were transfected with the bicistronic pCDH plasmid coding for GFP and either $PDIA1^{WT}$, $PDIA1^{D292N}$, $PDIA1^{R300H}$, $ERp57^{WT}$, $ERp57^{D217N}$, or $ERp57^{Q481K}$ using a $CaPO_4$ transfection protocol to reduce cell toxicity (Jiang & Chen, 2006; Sepulveda *et al*, 2010). Briefly, after 1 h of incubation at 5% CO_2, the cells were incubated for 20 min with transfection medium pre-equilibrated in a 10% CO_2 incubator to dissolve the DNA-$CaPO_4$ precipitates and then returned to a 5% CO_2 incubator. At 10 DIV, cells were fixed in 4% paraformaldehyde and immunostained with an antibody against MAP2 (1:400; Santa Cruz Biotechnology) to visualize all neurons (interneurons as well as motoneurons), and SMI-32 antibody (1:1,000 Convance) to identify motoneurons (Nagai *et al*, 2007; Fritz *et al*, 2013) (also see antibody list in the Appendix). Dendritic number and assessment of the length of each dendrite was performed as described previously (Sepulveda *et al*, 2010). Viability assays were performed as described in Fritz *et al* (2013).

The human embryonic stem cell (ESC) HuESC 3 Hb9::GFP line, where the coding sequence of GFP is under the control of Hb9 promoter restriction fragment, was described previously (Di Giorgio *et al*, 2008). Cells were differentiated as described in Di Giorgio *et al* (2008) with the sole modification that ES cells were grown under feeder-free conditions. Two days after plating differentiated neurons were transduced with lentivirus pseudotyped with VSGV envelope expressing $PDIA1^{WT}$, $PDIA1^{D292N}$, $PDIA1^{R300H}$, $ERp57^{WT}$, $ERp57^{D217N}$, and $ERp57^{Q481K}$, respectively, with a MOI of 10 viral particles per neuron, after transduction cells were cultured for another 10 days. To identify motor neurons after lentiviral transduction, immunocytochemistry analyses were performed as described in Lopez-Gonzalez *et al* (2009). Briefly, cells were washed three times with phosphate-buffered saline (PBS) and fixed with 4% paraformaldehyde for 20 min at room temperature. Cultures were washed three times with PBS and blocked by incubation with 10% bovine serum albumin (BSA)/0.3% Triton X-100 in PBS for 45 min. The following primary antibodies were used at the indicated dilutions in 10% BSA/PBS: rabbit anti-GFP 1:500 (Molecular Probes) and goat anti-choline acetyltransferase antibody (ChAT) 1:200 (Millipore), the secondary antibodies coupled with Alexa 488 or Alexa 568 (1:500; Molecular Probes) were used, and nuclei were stained with DAPI (Vector Labs). Quantification of axonal growth in the different experimental conditions of GFP- and ChAT-positive neurons was obtained using a Nikon TE2000-E2 microscope with a Yokogawa CSU10b spinning disk confocal scan head and custom laser launch, NEOS AOTF and relay optics (Solamere Technology Group, Salt Lake City, Utah).

Multiwavelength confocal z-series were acquired with a Nikon 20X Plan fluor oil objective (NA = 1.0) and a QImaging Rolera MGi camera using the standard digitizer. The final pixel size was 0.5388 μm/pixel, the *z* step was 0.3 μm, and the exposure time was 1 s per image. Metamorph Software controlled the microscope hardware and image acquisition. Dendritic number and assessment of the length of each dendrite were performed in the same manner as described above for primary rat motoneurons.

Immunoprecipitation

Immunoprecipitations (IP) were performed as previously described (Hetz *et al*, 2006). 293T cells were transfected using Effectene; after 48 h, cells were collected and washed once with 1 ml PBS, pH 7.4. Cells were resuspended in 500 μl NP-40 buffer (0.2% NP-40, 50 mM Tris/HCl pH 7.5, 150 mM NaCl, and protease inhibitor cocktail (Roche)) and incubated at 4°C overnight. After vortexing for 20 s, cell lysates were centrifuged at 10,000 rpm for 5 min at 4°C. The supernatant was incubated with anti-V5 antibody beads (V5 tagged Protein Purification Kit, MBL International) on a rotor wheel for 4 h at 4°C. Then, beads were washed three times with NP-40 buffer, increasing to 500 mM NaCl in the final wash. Protein complexes were eluted by adding V5 peptide (V5 tagged Protein Purification Kit, MBL International) for 30 min at room temperature. Input and eluates were analyzed by Western blot.

Biochemical blot analysis

Protein expression in NSC34 or N2a cells was performed as described previously (Hetz *et al*, 2009). Cells were lysed and homogenized by sonication in NP-40 buffer (50 mM Tris (pH 8.0), 150 mM NaCl, and 1% NP-40 containing a protease inhibitor cocktail from Roche (Basel, Switzerland)). Zebrafish embryos were lysed and homogenized in RIPA buffer (20 mM Tris (pH 8.0), 150 mM NaCl, 0.1% SDS, 0.5% DOC, and 0.5% Triton X-100 containing a protease inhibitor cocktail from Roche (Basel, Switzerland)). Murine cortex, spinal cord and muscle tissue were lysed and homogenized by sonication in NP-40 buffer (10 mM Tris (pH 8.0), 100 mM NaCl, 1 mM EDTA, and 1% NP-40 containing a protease inhibitor cocktail from Roche (Basel, Switzerland)) and phosphatase inhibitor cocktails 2 and 3 (Sigma-Aldrich). The following antibodies (see antibody list in the Appendix) and dilutions were used for Western blot: mouse anti-V5 1:5,000 (Invitrogen), rabbit anti-ERO1Lα 1:2,000 (Novus Biologicals), mouse anti-PDIA1 (1D3) 1:3,000 (Enzo), rabbit anti-PDIA1 (H-160) 1:1,000 (Santa Cruz), rabbit anti-ERp57 1:3,000 (Santa Cruz), rabbit anti-NMDAR2A 1:1,000 (Convance), mouse anti-synaptophysin 1:500 (Millipore), rabbit anti-PSD95 1:5,000 (Millipore), mouse anti-SV2 1:500 (Developmental Studies Hybridoma Bank), sheep anti-SOD1 1:3,000 (Calbiochem), rabbit anti-TDP43 1:2,000 (Proteintech), rabbit anti-β-actin-HRP conjugate 1:2,000 (Cell Signaling), goat anti-actin 1:1,000 (Santa Cruz), and rabbit anti-HSP90 1:3,000 (Santa Cruz). As secondary antibodies goat anti-rabbit HRP conjugate 1:3,000 (Invitrogen), rabbit anti-mouse HRP conjugate 1:3,000 (Invitrogen), donkey anti-sheep HRP conjugate 1:3,000 (Sigma-Aldrich), or rabbit anti-goat HRP conjugate 1:3,000 (Invitrogen) were used.

PNGase F treatment was performed according to the manufacturer's instructions. Briefly, 20 μg of N2a cell extract was digested for 2 h at 37°C. Protein samples were prepared using standard procedures. Five micrograms was loaded onto 10% PAA-minigels and subsequently Western blotted. V5-tagged proteins were detected with mouse anti-V5 (1:15,000). BDNF detection in cell supernatant was performed by transiently co-transfecting N2a cells with BDNF-GFP (Haubensak *et al*, 1998) and PDIs. Cells were grown in normal culture medium containing 10% FBS. About 200 μl of media was collected after 18 and 30 h after gently swirling. Media were centrifuged at 11,000 *g* for 5 min to remove cell debris. Typically, 40 μl of media was run in the SDS–PAGE without any concentration step. BDNF-GFP was detected after Western blot using anti-GFP (1:3,000). Protein extracts were also analyzed by filter trap was performed as recently reported (Torres *et al*, 2015). RNA purification and real-time PCR were performed as previously described (Lisbona *et al*, 2009) using the following primers: *actin* forward 5′-TACCACCATGTACCCAGGCA-3′, *actin* reverse 5′-CTCAG GAGGAGCAATGATCTTGAT-3′, *erp57* forward 5′-GAGGCTTGCCCC TGAGTATG-3′, and *erp57* reverse 5′-GTTGGCAGTGCAATCCACC-3′.

Analysis of zebrafish axonal motoneuron morphology and detection of NMJ

Wild-type *Tübingen* and transgenic *Tg(HuC:Kaede)* (Sato *et al*, 2006) *z*ebrafish (*Danio rerio*) strains were maintained, crossed, injected, raised, and staged as described (Sato *et al*, 2006). Animal experimentation protocols were approved by the Bioethics Committee of the Faculty of Medicine at the University of Chile. For *in vitro* synthesis of capped RNA with the T7 mMESSAGE mMACHINE system (Ambion), pcDNA3.1/V5-based constructs (version of the human $PDIA1^{WT}$, $PDIA1^{R300H}$, $PDIA1^{D292N}$, $ERp57^{WT}$, $ERp57^{D217N}$, and $ERp57^{Q418K}$) were linearized with StuI. For overexpression experiments, zebrafish embryos were microinjected at one-cell stage with sense mRNA diluted in water, using a Picospritzer III (general valve) pressure ejector. After testing different doses, the final mRNA concentrations used were 80 pg/embryo for PDIA1 ($PDIA1^{WT}$, $PDIA1^{D292N}$, and PDI^{R300H}) or 30 pg/embryo for ERp57 ($ERp57^{WT}$, $ERp57^{D217N}$, and $ERp57^{Q418K}$) (Appendix Table S1). Global overexpression phenotypes were analyzed at 60–70% epiboly and 24 hpf in an SMZ-1000 Nikon stereomicroscope.

For analysis of axonal projections of motoneurons, microinjected *Tg(HuC::Kaede)* zebrafish embryos with PDI mutants and wild-type controls mRNA were anesthetized with tricaine (Sigma-Aldrich) at 36 hpf, and mounted in agarose for spinning disk confocal microscopic observation and photography. Image acquisition was performed with Volocity software (PerkinElmer). Axonal projections of motoneurons at a defined location in the spinal cord were determined as previously described (Kabashi *et al*, 2009, 2011). Analysis of Z-stacks by confocal microscopy was performed in three to four traced axonal projections per embryo. The axonal lengths of the labeled axon from the spinal cord were traced to their first branching point using ImageJ software. These values were averaged for each of the embryos analyzed (6–10 zebrafish per condition). For immunostaining, mRNA-injected embryos were fixed at 72 hpf in 4% paraformaldehyde/PBS overnight at 4°C and washed three times in PBS for 10 min. After 20 min of 2.5% trypsin treatment, embryos were immunoassayed using mouse anti-SV2 (1:200; Development Studies Hybridoma Bank), followed by incubation with Alexa 568-conjugated goat anti-mouse antibody (1:200; Molecular Probes),

and Alexa 488-conjugated α-bungarotoxin (1:100; Molecular Probes) according to established protocols (Wang *et al*, 2008). Fluorescent images of fixed embryos were taken using a Fluoview1000 Spectral confocal microscope (Olympus®) and Plan-Apochromat 20x and 40x/1.0 W lenses. Images were processed with ImageJ (http://rsb-web.nih.gov/ij/), Volocity (Improvision), and Adobe Photoshop CS3 (Adobe) softwares.

Touch-evoked responses were assessed on a 1.5-zoom stereomicroscope (Kyoto Optical) as described previously (Kabashi *et al*, 2009, 2011). Briefly, in order to induce escape-swimming response, embryos at 48 hpf were stimulated lightly by touching them at the level of the tail using a gel-loading tip, their responses recorded with a VL-Z7U digital video camera (Sharp) at 30 frames/s.

Recombinant proteins and biochemical characterization

Proteins were expressed in *E. coli* strain BL21 (DE3) pLysS or pLysS-RARE grown in autoinduction media. His-tagged proteins were purified by immobilized metal affinity chromatography and ion exchange chromatography as described previously (Lappi *et al*, 2004). Purified proteins were checked for authenticity by mass spectrometry, and the concentrations were calculated based on their calculated molar extinction coefficients. Far UV CD spectra of proteins and thermal denaturation were performed with Chirascan Plus CD Spectrometer (Applied Photophysics, UK). Protein concentration was 100 μg/ml, and the measurements were carried out in 20 mM phosphate buffer pH 7.3 with five repeats over 195–250 nm using a cell with a path length of 10 mm, a spectral bandwidth of 1 nm, and a time constant of 0.5 s. Thermal denaturation was done with temperature range from 22 to 92°C with smooth temperature ramp of 1°C/min using TC125 temperature controller (Quantum Northwest, Liberty Lake, WA, USA). All spectra were corrected for the blank spectra with no protein added, and the thermal denaturation was analyzed calculating the change in spectra at 220 nm.

SPR measurements were performed with Biacore T200 (GE Healthcare, Uppsala, Sweden). CRT P domain in 10 mM acetate pH 4.5 was immobilized onto CM5 chip (GE Healthcare) using amine coupling according to manufacturer's instructions. The immobilization level was approximately 1,000 RU. The binding of ERp57 wild type and mutants was analyzed in 20 mM phosphate buffer pH 7.3 with concentration range from 0 to 1 μM of protein, at flow rate 30 μl/min and contact time 120 s at 25°C. Washing for 10 min with running buffer was enough for regeneration. Limited proteolysis was carried out in 20 mM phosphate buffer pH 7.3 in the presence of 10 mM β-mercaptoethanol. About 10 μM protein was incubated with or without 10 μg/ml proteinase K (Roche, Indianapolis, IN, USA) for 30 min at 25°C (for ERp57) or at 4°C (for PDIA1). The reaction was stopped with 5 mM PMSF (Sigma-Aldrich, St. Louis, MO, USA). Protein fragments were separated on SDS–PAGE. Desired peptide fragments were cut out from the gel and analyzed by mass spectrometry after in-gel trypsin digestion. In addition, total sample mixtures were analyzed by mass spectrometry. Fluorescence spectra were measured on FluoroMax-4 (HORIBA Instruments, Edison, NJ, USA) with 1 μM PDIA1 b′x wild type and mutants in 20 mM phosphate buffer pH 7.3. Shifts in fluorescence ratios (331–337 nm/352–358 nm) were calculated as described previously (Nguyen *et al*, 2008).

BPTI was purified as described previously (Nguyen *et al*, 2008). Pure reduced BPTI was lyophilized and resuspended into 10 mM HCl pH 2.0 to prevent oxidative refolding. The BPTI refolding was carried out as described previously (Karala *et al*, 2009) with the exception that the reaction was stopped by the addition of 50 mM NEM. Samples were diluted 1:10 in 0.1% TFA and analyzed by ESI-mass spectrometry (Synapt G2, Waters, Milford, MA, USA) coupled to ACQUITY UPLC machinery (Waters) with BEH300 C4 1.7 μm 2.1 × 10 mm UPLC column for desalting and protein separation prior mass spectrometric analysis. UPLC was performed using 0.4 ml/min flow with 0.1% formic acid and 3% to 40% acetonitrile gradient over 15 min.

Generation of conditional ERp57 knockout mice

The ERp57 floxed mice were previously described where exons 2 and 3 were flanked with two *lox*P sites(Garbi *et al*, 2006) and were kindly provided by Dr. Günther Hämmerling (German Cancer Research Center, Heidelberg, Germany). Mice expressing Cre recombinase under the control of the nestin promoter were obtained from The Jackson Laboratory (B6.Cg-Tg(Nes-cre)1Kln/J, 003771). To generate mice deficient in ERp57 in the central nervous system (CNS), ERp57 floxed mice were crossed with Nestin-Cre transgenic mice as we described before (Hetz *et al*, 2008), and generated offspring carrying the floxed or knockout allele in heterozygous or homozygous form designated as follows: $ERp57^{WT}$ (wild type), $ERp57^{Nes+/-}$ (heterozygous), and $ERp57^{Nes-/-}$ (conditional knockout). All experiments and animal care follows the Institutional Review Board's Animal Care of the University of Chile (CBA # 0305 FMUCH). The following primers were used for genotyping of mice: *erp57* floxed allele, forward 5′-CGCCAGCCTCTCCATTTAG -3′; *erp57* floxed reverse 5′-CAGAGATCCTGCCTCTG-3′, Cre forward 5′-GC GGTCTGGCAGTAAAAACTATC-3′, and Cre reverse 5′-GTGAAA CAGCATTGCTGTCACTT-3′.

Beginning at 24 days of age, mice were evaluated weekly by three criteria for the onset of motor neuron defects and disease symptoms: (i) weight, (ii) rotarod performance, and (iii) hanging test. Rotarod test was performed as previously described (Vidal *et al*, 2012). In brief, mice were placed into a rod rotating (Model LE8500, Panlab SL) at a constant speed of 4 rpm. The time until mice fell from the rod was measured until 120 s. Mice were first trained three times per day for five consecutive days. The hanging test was described previously (Klein *et al*, 2011).

Electromyography (EMG)

Animals were anesthetized with avertin and placed in a prone position on a thermal pad at 37°C for the examination. EMG recordings using a Cardinal Synergy electromyography (EMG) machine were obtained with a 30G needle using a gain of 50 μV/division and a band pass filter with low and high cutoff frequency settings of 20 and 10,000 Hz, respectively. Potentials were recorded from several sites of the hindlimb muscles with a concentric needle electrode (30G). A ground self-adhesive gelled surface electrode was placed over the tail. The recording electrode was inserted into the tibialis anterior (TA) or gastrocnemius/soleus muscles, and spontaneous electrical activity was recorded for 90 s. The procedure took 15–20 min per mouse, after which the mice were euthanized.

Immunohistochemistry

Histological analysis was performed as previously described (Valenzuela *et al*, 2012). Mice were anesthetized deeply with 33 μl/g of 10 mg/ml avertin in 0.1 M saline phosphate buffer (PBS) and perfused transcardially with 4% paraformaldehyde. Spinal cords were collected and transversally sectioned (20-μm-thick slices) using a cryostat microtome (Leica, Nussloch, Germany). Sections were immunostained using the antibodies NeuN 1:600 (MAB377, Millipore Bioscience Research Reagents) and GFAP 1:1,000 (N1506, Dako). Tissue sections were viewed with an Olympus IX71 microscope, and images were captured using a QImaging QICAM Fast 1394 camera. Neuronal numbers were assessed by counting NeuN-positive cells in the ventral horn.

In addition, calbindin staining was performed in cerebellum sections using standard methods. Tissue was incubated with anti-calbindin 1:200 (Cell Signaling) for 16 h at 4°C and developed with an anti-rabbit IgG (Vectastain) and DAB (Sigma Chemical Company) using instruction of the manufacturer. Tissue sections were viewed with a Nikon Eclipse 80*i* microscope, and images were captured using a Nikon DS-*Fi*1 camera.

Skeletal muscle staining

Whole-mounted diaphragms were dissected out and fixed in 4% PFA for 1 h at 4°C. Samples were first permeabilized in 0.5% Triton X-100 and treated with 0.1 M glycine, pH 7.4, for 15 min and then blocked in 2% BSA and 0.5% horse serum, for 12–16 h. Muscles were incubated with a rabbit anti-neurofilament antibody (Abcam, Cambridge, UK) (1:1,000), for 12–16 h and then with a Cy3-conjugated donkey anti-rabbit antibody (Jackson Immuno Research, West Grove, PA) (1:300) plus Alexa488-conjugated α-bungarotoxin (α-BTX) (Invitrogen, Carlsbad, CA) (1:1,000) for 12–16 h. Samples were flat mounted between two coverslips and imaged. *Tibialis anterior* muscles were removed, mounted in OCT (Sakura Finetek, Torrance, CA, USA), and quickly frozen in liquid nitrogen-cooled isopentane. Cryosections (20 μm) were fixed with 4% paraformaldehyde for 20 min at room temperature and subsequently processed. Muscle fiber morphology was analyzed with conventional hematoxylin/chromotrope staining, whereas fibrosis was analyzed by staining collagen depositions with a 1% Bismarck Brown aqueous solution for 12 min. Samples were mounted in Entellan medium (Merck, Darmstadt, Germany). To analyze muscle regeneration, cold methanol-fixed cryosections were stained with 1 μg/ml Alexa488-conjugated wheat germ agglutinin (Invitrogen) and 0.3 μM DAPI. Cryosections were also stained with a NADH reduced solution (Tris–buffer, pH 7.4, NADH reduced, nitro-blue tetrazolium) (Sigma, St. Louis, MO, USA) for 45 min, and fibers were classified into slow twitch (dark blue), intermediate (blue), and fast twitch (light blue). The identity and diameter of > 100 fibers per type were determined using ImageJ software and are expressed as the percentage of the total.

NMJ analyses

For endplate band quantification, fluorescent images of α-BTX-stained right hemidiaphragms were captured with a Nikon Eclipse 80i fluorescent microscope, and AChR cluster distribution was analyzed. The endplate bandwidth of 20–40 bins per animal, obtained every 134 μm at the central region of each hemidiaphragm was measured with ImageJ. To analyze postsynaptic morphologies, *z*-stack pictures were imaged at 1-μm intervals with a Zeiss LSM 780 confocal microscope at the CMA Bio-Bio facility, University of Concepcion, Chile. Maximal intensity projections images were reconstructed in 3D using ImageJ software and analyzed to determine the proportion of the different NMJ morphologies, grouped into "pretzels", normal shapes with continuous stripes, "fragmented", where pretzels are separated into > 4 fragments, "O" or "C" shaped, less complex postsynaptic densities with no internal stripes, and "dismantled", structures with a shrinked shape. The morphology of > 200 NMJs was manually determined and expressed as the percentage of the total. The area and perimeter of > 60 AChR densities per animal were automatically determined in a 60 μm^2 ROI for each postsynaptic structure using ImageJ software. Representative 3D videos where acquired with Imaris Scene Viewer 7.6.4 software (Bitplane, Zurich, Switzerland).

Protein sequence and structural analysis

Structural analysis was performed using the SWISSMODEL server (http://swissmodel.expasy.org/) and Chimera1.6.1 imaging software. The PDB structure 3uem (Wang *et al*, 2012) was used as a template to model PDIA1 mutants, whereas for ERp57 mutants, the PDB structure 3f8u (Dong *et al*, 2009) was used.

Statistical analysis

For statistical analysis GraphPad Prism Software version 5.01 was used. All graphs show mean with SEM. Significance was calculated using Student's *t*-test, one-way ANOVA, or two-way ANOVA with Bonferroni's *post hoc* test.

Expanded View for this article is available online.

Acknowledgements
We thank Dr. Miklos Geiszt (Semmelweis University, Hungary) for providing HyPer-ER vectors and Dr. Neil Bulleid (University of Glasgow, Scotland) for providing PDIA1-V5 and ERp57-V5 plasmids. We thank Dr. Günter Hämmerling (German Cancer Research Center, Germany) for kindly providing the floxed ERp57 mice. We thank Silke Escobar, Javiera Ponce, Claudia Molina, Alvaro Diaz, and Ulrich Bergmann for technical assistance. This work was primarily funded by the Frick Foundation, Muscular Dystrophy Association 382453 in addition to ALS Therapy Alliance 2014-F-059, Millennium Institute No. P09-015-F, CONICYT-USA2013-0003 (to C.H.) and Ring Initiative ACT1109 grants (to C.H. and P.H.) and FONDAP 15150012 (to C.H., S.M., R.L.V.) and FONDECYT no. 3110067 and 1150743 (to U.W.), FONDECYT no. 3130351 and 11150579 (to D.B.M.), and FONDECYT no. 1150608 (to R.L.V.). We also received support from the Michael J Fox Foundation for Parkinson's Research, COPEC-UC Foundation, FONDEF no. D11I1007 and FONDECYT no. 1140549, Office of Naval Research-Global (ONR-G) N62909-16-1-2003 and ALSRP Therapeutic Idea Award AL150111 (all to C.H.), FONDECYT no. 11090324 (to A.C.); FONDECYT 1140301, DRI-USA 2013-0030 and Ring Initiative ACT1114 (to B.v.Z.), Millennium Institute No. P09-015-F and Howard Hughes Medical Institute (HHMI INTNL 55005940) (to M.C.); ALS Therapy Alliance and the NIH (NS057553-07) (to F.B.G.), CONICYT Doctoral fellowship (to M.T., A.D., J.O., V.P., and V.V.), CONICYT

24110099 (to F.J.B.); FONDECYT 1130321 and MINREB Millennium Nucleus RC120003 (to J.P.H.), FONDECYT no. 1110433 (to P.H.). R.H.B. is supported by ALS Therapy Alliance, Project ALS, P2ALS, the Angel Fund, the Pierre L. de Bourgknecht ALS Research Foundation, the Al-Athel ALS Research Foundation, the ALS Family Charitable Foundation and NIH/NINDS 1R01NS050557. P.G.-P. was supported by the Alfonso Martin Escudero Foundation (Madrid). M.J.S. and L.W.R. were supported by Biocenter Oulu, Finland.

Author contributions

PG-P discovered and cloned PDI variants into expression vector. MJS and LWR performed *in vitro* structural and biochemical studies. UW performed immunoprecipitation experiments. UW, AS, and RA performed HyperER experiments. SM and NM performed PDI knockdown experiment. RLV and UW performed colocalization studies. SA performed ELISA. AC, KP, RA, and UW performed zebrafish phenotypical analysis. UW, FJB, RL-G, and PR performed motoneuron outgrowth studies and morphological analysis. UW, CIA, TI, and MT maintained and generated the ERp57 knockout mice and performed their behavioral analysis. JO, VP, and JPH performed NMJ and muscle analyses. VV performed spinal cord histology. UW, DBM, and PR performed cortex, spinal cord, and muscle protein analysis. PH and SF-C performed spinal cord stereology. JS and MC performed EMG measurements. UW managed and collected all data and conducted statistical analysis. UW, CH, RHB, BvZ, F-BG, MLC, LWR, and JPH designed and supervised the experiments. UW and CH wrote the manuscript. RHB, BvZ, F-BG, MLC, LWR, and JPH revised and edited the manuscript.

Conflict of interest

The authors declare that they have no conflict of interest.

References

Andreu CI, Woehlbier U, Torres M, Hetz C (2012) Protein disulfide isomerases in neurodegeneration: from disease mechanisms to biomedical applications. *FEBS Lett* 586: 2826 – 2834

Appenzeller-Herzog C, Riemer J, Zito E, Chin KT, Ron D, Spiess M, Ellgaard L (2010) Disulphide production by Ero1alpha-PDI relay is rapid and effectively regulated. *EMBO J* 29: 3318 – 3329

Armstrong GA, Drapeau P (2013) Loss and gain of FUS function impair neuromuscular synaptic transmission in a genetic model of ALS. *Hum Mol Genet* 22: 4282 – 4292

Atkin JD, Farg MA, Turner BJ, Tomas D, Lysaght JA, Nunan J, Rembach A, Nagley P, Beart PM, Cheema SS, Horne MK (2006) Induction of the unfolded protein response in familial amyotrophic lateral sclerosis and association of protein-disulfide isomerase with superoxide dismutase 1. *J Biol Chem* 281: 30152 – 30165

Atkin JD, Farg MA, Walker AK, McLean C, Tomas D, Horne MK (2008) Endoplasmic reticulum stress and induction of the unfolded protein response in human sporadic amyotrophic lateral sclerosis. *Neurobiol Dis* 30: 400 – 407

Babin PJ, Goizet C, Raldua D (2014) Zebrafish models of human motor neuron diseases: advantages and limitations. *Prog Neurobiol* 118: 36 – 58

Bernard-Marissal N, Sunyach C, Marissal T, Raoul C, Pettmann B (2014) Calreticulin levels determine onset of early muscle denervation by fast motoneurons of ALS model mice. *Neurobiol Dis* 73: 130 – 136

Bernard-Marissal N, Sunyach C, Marissal T, Raoul C, Pettmann B (2015) Calreticulin levels determine onset of early muscle denervation by fast motoneurons of ALS model mice. *Neurobiol Dis* 73: 130 – 136

Castillo V, Onate M, Woehlbier U, Rozas P, Andreu C, Medinas D, Valdes P, Osorio F, Mercado G, Vidal RL, Kerr B, Court FA, Hetz C (2015) Functional Role of the Disulfide Isomerase ERp57 in Axonal Regeneration. *PLoS One* 10: e0136620

Chen H, Qian K, Du Z, Cao J, Petersen A, Liu H, Blackbourn LWT, Huang CL, Errigo A, Yin Y, Lu J, Ayala M, Zhang SC (2014) Modeling ALS with iPSCs reveals that mutant SOD1 misregulates neurofilament balance in motor neurons. *Cell Stem Cell* 14: 796 – 809

Di Giorgio FP, Boulting GL, Bobrowicz S, Eggan KC (2008) Human embryonic stem cell-derived motor neurons are sensitive to the toxic effect of glial cells carrying an ALS-causing mutation. *Cell Stem Cell* 3: 637 – 648

Dong G, Wearsch PA, Peaper DR, Cresswell P, Reinisch KM (2009) Insights into MHC class I peptide loading from the structure of the tapasin-ERp57 thiol oxidoreductase heterodimer. *Immunity* 30: 21 – 32

Douglas PM, Dillin A (2010) Protein homeostasis and aging in neurodegeneration. *J Cell Biol* 190: 719 – 729

Dupuis L, Gonzalez de Aguilar JL, Echaniz-Laguna A, Eschbach J, Rene F, Oudart H, Halter B, Huze C, Schaeffer L, Bouillaud F, Loeffler JP (2009) Muscle mitochondrial uncoupling dismantles neuromuscular junction and triggers distal degeneration of motor neurons. *PLoS One* 4: e5390

Ellgaard L, Ruddock LW (2005) The human protein disulphide isomerase family: substrate interactions and functional properties. *EMBO Rep* 6: 28 – 32

Enyedi B, Varnai P, Geiszt M (2010) Redox state of the endoplasmic reticulum is controlled by Ero1L-alpha and intraluminal calcium. *Antioxid Redox Signal* 13: 721 – 729

Farg MA, Soo KY, Walker AK, Pham H, Orian J, Horne MK, Warraich ST, Williams KL, Blair IP, Atkin JD (2012) Mutant FUS induces endoplasmic reticulum stress in amyotrophic lateral sclerosis and interacts with protein disulfide-isomerase. *Neurobiol Aging* 33: 2855 – 2868

Feige MJ, Hendershot LM (2011) Disulfide bonds in ER protein folding and homeostasis. *Curr Opin Cell Biol* 23: 167 – 175

Ferraiuolo L, Kirby J, Grierson AJ, Sendtner M, Shaw PJ (2011) Molecular pathways of motor neuron injury in amyotrophic lateral sclerosis. *Nat Rev Neurol* 7: 616 – 630

Filezac de L'Etang A, Maharjan N, Cordeiro Brana M, Ruegsegger C, Rehmann R, Goswami A, Roos A, Troost D, Schneider BL, Weis J, Saxena S (2015) Marinesco-Sjogren syndrome protein SIL1 regulates motor neuron subtype-selective ER stress in ALS. *Nat Neurosci* 18: 227 – 238

Fritz E, Izaurieta P, Weiss A, Mir FR, Rojas P, Gonzalez D, Rojas F, Brown RH, Madrid R, van Zundert B (2013) Mutant SOD1-expressing astrocytes release toxic factors that trigger motor neuron death by inducing hyperexcitability. *J Neurophysiol* 109: 2803 – 2814

Garbi N, Tanaka S, Momburg F, Hammerling GJ (2006) Impaired assembly of the major histocompatibility complex class I peptide-loading complex in mice deficient in the oxidoreductase ERp57. *Nat Immunol* 7: 93 – 102

Gonzalez-Perez P, Woehlbier U, Chian RJ, Sapp P, Rouleau GA, Leblond CS, Daoud H, Dion PA, Landers JE, Hetz C, Brown RH (2015) Identification of rare protein disulfide isomerase gene variants in amyotrophic lateral sclerosis patients. *Gene* 566: 158 – 165

Grek C, Townsend DM (2014) Protein disulfide isomerase superfamily in disease and the regulation of apoptosis. *Endoplasmic Reticulum Stress Dis* 1: 4 – 17

Hahm E, Li J, Kim K, Huh S, Rogelj S, Cho J (2013) Extracellular protein disulfide isomerase regulates ligand-binding activity of alphaMbeta2 integrin and neutrophil recruitment during vascular inflammation. *Blood* 121: 3789 – 3800, S3781–3715

Hatahet F, Ruddock LW (2009) Protein disulfide isomerase: a critical evaluation of its function in disulfide bond formation. *Antioxid Redox Signal* 11: 2807 – 2850

Haubensak W, Narz F, Heumann R, Lessmann V (1998) BDNF-GFP containing secretory granules are localized in the vicinity of synaptic junctions of cultured cortical neurons. *J Cell Sci* 111(Pt 11): 1483 – 1493

Hetz C, Bernasconi P, Fisher J, Lee AH, Bassik MC, Antonsson B, Brandt GS, Iwakoshi NN, Schinzel A, Glimcher LH, Korsmeyer SJ (2006) Proapoptotic BAX and BAK modulate the unfolded protein response by a direct interaction with IRE1alpha. *Science* 312: 572 – 576

Hetz C, Lee AH, Gonzalez-Romero D, Thielen P, Castilla J, Soto C, Glimcher LH (2008) Unfolded protein response transcription factor XBP-1 does not influence prion replication or pathogenesis. *Proc Natl Acad Sci USA* 105: 757 – 762

Hetz C, Thielen P, Matus S, Nassif M, Court F, Kiffin R, Martinez G, Cuervo AM, Brown RH, Glimcher LH (2009) XBP-1 deficiency in the nervous system protects against amyotrophic lateral sclerosis by increasing autophagy. *Genes Dev* 23: 2294 – 2306

Hetz C (2012) The unfolded protein response: controlling cell fate decisions under ER stress and beyond. *Nat Rev Mol Cell Biol* 13: 89 – 102

Hetz C, Chevet E, Harding H (2013) Targeting the unfolded protein response in disease. *Nat Rev Drug Discov* 12: 703 – 719

Hetz C, Mollereau B (2014) Disturbance of endoplasmic reticulum proteostasis in neurodegenerative diseases. *Nat Rev Neurosci* 15: 233 – 249

Hirsch I, Weiwad M, Prell E, Ferrari DM (2014) ERp29 deficiency affects sensitivity to apoptosis via impairment of the ATF6-CHOP pathway of stress response. *Apoptosis* 19: 801 – 815

Hoffstrom BG, Kaplan A, Letso R, Schmid RS, Turmel GJ, Lo DC, Stockwell BR (2010) Inhibitors of protein disulfide isomerase suppress apoptosis induced by misfolded proteins. *Nat Chem Biol* 6: 900 – 906

Honjo Y, Kaneko S, Ito H, Horibe T, Nagashima M, Nakamura M, Fujita K, Takahashi R, Kusaka H, Kawakami K (2011) Protein disulfide isomerase-immunopositive inclusions in patients with amyotrophic lateral sclerosis. *Amyotroph Lateral Scler* 12: 444 – 450

Hosoda A, Tokuda M, Akai R, Kohno K, Iwawaki T (2010) Positive contribution of ERdj5/JPDI to endoplasmic reticulum protein quality control in the salivary gland. *Biochem J* 425: 117 – 125

Ilieva EV, Ayala V, Jove M, Dalfo E, Cacabelos D, Povedano M, Bellmunt MJ, Ferrer I, Pamplona R, Portero-Otin M (2007) Oxidative and endoplasmic reticulum stress interplay in sporadic amyotrophic lateral sclerosis. *Brain* 130: 3111 – 3123

Jaronen M, Goldsteins G, Koistinaho J (2014) ER stress and unfolded protein response in amyotrophic lateral sclerosis-a controversial role of protein disulphide isomerase. *Front Cell Neurosci* 8: 402

Jessop CE, Chakravarthi S, Garbi N, Hammerling GJ, Lovell S, Bulleid NJ (2007) ERp57 is essential for efficient folding of glycoproteins sharing common structural domains. *EMBO J* 26: 28 – 40

Jessop CE, Watkins RH, Simmons JJ, Tasab M, Bulleid NJ (2009) Protein disulphide isomerase family members show distinct substrate specificity: P5 is targeted to BiP client proteins. *J Cell Sci* 122: 4287 – 4295

Jiang M, Chen G (2006) High Ca2+-phosphate transfection efficiency in low-density neuronal cultures. *Nat Protoc* 1: 695 – 700

Jin H, Mimura N, Kashio M, Koseki H, Aoe T (2014) Late-onset of spinal neurodegeneration in knock-in mice expressing a mutant BiP. *PLoS One* 9: e112837

Kabashi E, Lin L, Tradewell ML, Dion PA, Bercier V, Bourgouin P, Rochefort D, Bel Hadj S, Durham HD, Vande Velde C, Rouleau GA, Drapeau P (2009) Gain and loss of function of ALS-related mutations of TARDBP (TDP-43) cause motor deficits in vivo. *Hum Mol Genet* 19: 671 – 683

Kabashi E, Champagne N, Brustein E, Drapeau P (2010) In the swim of things: recent insights to neurogenetic disorders from zebrafish. *Trends Genet* 26: 373 – 381

Kabashi E, Bercier V, Lissouba A, Liao M, Brustein E, Rouleau GA, Drapeau P (2011) FUS and TARDBP but not SOD1 interact in genetic models of amyotrophic lateral sclerosis. *PLoS Genet* 7: e1002214

Karala AR, Lappi AK, Saaranen MJ, Ruddock LW (2009) Efficient peroxide-mediated oxidative refolding of a protein at physiological pH and implications for oxidative folding in the endoplasmic reticulum. *Antioxid Redox Signal* 11: 963 – 970

Kiskinis E, Sandoe J, Williams LA, Boulting GL, Moccia R, Wainger BJ, Han S, Peng T, Thams S, Mikkilineni S, Mellin C, Merkle FT, Davis-Dusenbery BN, Ziller M, Oakley D, Ichida J, Di Costanzo S, Atwater N, Maeder ML, Goodwin MJ *et al* (2014) Pathways disrupted in human ALS motor neurons identified through genetic correction of mutant SOD1. *Cell Stem Cell* 14: 781 – 795

Klein A, Mosqueira M, Martinez G, Robledo F, Gonzalez M, Caballero B, Cancino GI, Alvarez AR, Hetz C, Zanlungo S (2011) Lack of activation of the unfolded protein response in mouse and cellular models of Niemann-Pick type C disease. *Neurodegener Dis* 8: 124 – 128

Kozlov G, Maattanen P, Schrag JD, Pollock S, Cygler M, Nagar B, Thomas DY, Gehring K (2006) Crystal structure of the bb' domains of the protein disulfide isomerase ERp57. *Structure* 14: 1331 – 1339

Kraus A, Groenendyk J, Bedard K, Baldwin TA, Krause KH, Dubois-Dauphin M, Dyck J, Rosenbaum EE, Korngut L, Colley NJ, Gosgnach S, Zochodne D, Todd K, Agellon LB, Michalak M (2010) Calnexin deficiency leads to dysmyelination. *J Biol Chem* 285: 18928 – 18938

Kwok CT, Morris AG, Frampton J, Smith B, Shaw CE, de Belleroche J (2013) Association studies indicate that protein disulfide isomerase is a risk factor in amyotrophic lateral sclerosis. *Free Radic Biol Med* 58: 81 – 86

Lappi AK, Lensink MF, Alanen HI, Salo KE, Lobell M, Juffer AH, Ruddock LW (2004) A conserved arginine plays a role in the catalytic cycle of the protein disulphide isomerases. *J Mol Biol* 335: 283 – 295

Leblond CS, Kaneb HM, Dion PA, Rouleau GA (2014) Dissection of genetic factors associated with amyotrophic lateral sclerosis. *Exp Neurol* 262 Pt B: 91 – 101

Lee YB, Chen HJ, Peres JN, Gomez-Deza J, Attig J, Stalekar M, Troakes C, Nishimura AL, Scotter EL, Vance C, Adachi Y, Sardone V, Miller JW, Smith BN, Gallo JM, Ule J, Hirth F, Rogelj B, Houart C, Shaw CE (2013) Hexanucleotide repeats in ALS/FTD form length-dependent RNA foci, sequester RNA binding proteins, and are neurotoxic. *Cell Rep* 5: 1178 – 1186

Li Y, Camacho P (2004) Ca2+-dependent redox modulation of SERCA 2b by ERp57. *J Cell Biol* 164: 35 – 46

Ling SC, Polymenidou M, Cleveland DW (2013) Converging Mechanisms in ALS and FTD: disrupted RNA and Protein Homeostasis. *Neuron* 79: 416 – 438

Lisbona F, Rojas-Rivera D, Thielen P, Zamorano S, Todd D, Martinon F, Glavic A, Kress C, Lin JH, Walter P, Reed JC, Glimcher LH, Hetz C (2009) BAX inhibitor-1 is a negative regulator of the ER stress sensor IRE1alpha. *Mol Cell* 33: 679 – 691

Liu JX, Brannstrom T, Andersen PM, Pedrosa-Domellof F (2013) Distinct changes in synaptic protein composition at neuromuscular junctions of extraocular muscles versus limb muscles of ALS donors. *PLoS One* 8: e57473

Lopez-Gonzalez R, Kunckles P, Velasco I (2009) Transient recovery in a rat model of familial amyotrophic lateral sclerosis after transplantation of

motor neurons derived from mouse embryonic stem cells. *Cell Transplant* 18: 1171 – 1181

Ma T, Trinh MA, Wexler AJ, Bourbon C, Gatti E, Pierre P, Cavener DR, Klann E (2013) Suppression of eIF2alpha kinases alleviates Alzheimer's disease-related plasticity and memory deficits. *Nat Neurosci* 16: 1299 – 1305

Maattanen P, Gehring K, Bergeron JJ, Thomas DY (2010) Protein quality control in the ER: the recognition of misfolded proteins. *Semin Cell Dev Biol* 21: 500 – 511

Mardones P, Martinez G, Hetz C (2015) Control of systemic proteostasis by the nervous system. *Trends Cell Biol* 25: 1 – 10

Matus S, Lopez E, Valenzuela V, Nassif M, Hetz C (2013b) Functional contribution of the transcription factor ATF4 to the pathogenesis of amyotrophic lateral sclerosis. *PLoS One* 8: e66672

Matus S, Medinas DB, Hetz C (2014) Common ground: stem cell approaches find shared pathways underlying ALS. *Cell Stem Cell* 14: 697 – 699

Matus S, Valenzuela V, Medinas DB, Hetz C (2013a) ER dysfunction and protein folding stress in ALS. *Int J Cell Biol* 2013: 674751

Moreno JA, Radford H, Peretti D, Steinert JR, Verity N, Martin MG, Halliday M, Morgan J, Dinsdale D, Ortori CA, Barrett DA, Tsaytler P, Bertolotti A, Willis AE, Bushell M, Mallucci GR (2012) Sustained translational repression by eIF2alpha-P mediates prion neurodegeneration. *Nature* 485: 507 – 511

Nagai M, Re DB, Nagata T, Chalazonitis A, Jessell TM, Wichterle H, Przedborski S (2007) Astrocytes expressing ALS-linked mutated SOD1 release factors selectively toxic to motor neurons. *Nat Neurosci* 10: 615 – 622

Nardo G, Pozzi S, Pignataro M, Lauranzano E, Spano G, Garbelli S, Mantovani S, Marinou K, Papetti L, Monteforte M, Torri V, Paris L, Bazzoni G, Lunetta C, Corbo M, Mora G, Bendotti C, Bonetto V (2011) Amyotrophic lateral sclerosis multiprotein biomarkers in peripheral blood mononuclear cells. *PLoS One* 6: e25545

Nemere I, Garbi N, Hammerling GJ, Khanal RC (2010) Intestinal cell calcium uptake and the targeted knockout of the 1,25D3-MARRS (membrane-associated, rapid response steroid-binding) receptor/PDIA3/Erp57. *J Biol Chem* 285: 31859 – 31866

Nguyen VD, Wallis K, Howard MJ, Haapalainen AM, Salo KE, Saaranen MJ, Sidhu A, Wierenga RK, Freedman RB, Ruddock LW, Williamson RA (2008) Alternative conformations of the x region of human protein disulphide-isomerase modulate exposure of the substrate binding b' domain. *J Mol Biol* 383: 1144 – 1155

Oakes SA, Papa FR (2015) The role of endoplasmic reticulum stress in human pathology. *Annu Rev Pathol* 10: 173 – 194

Park SW, Zhen G, Verhaeghe C, Nakagami Y, Nguyenvu LT, Barczak AJ, Killeen N, Erle DJ (2009) The protein disulfide isomerase AGR2 is essential for production of intestinal mucus. *Proc Natl Acad Sci USA* 106: 6950 – 6955

Patten SA, Armstrong GA, Lissouba A, Kabashi E, Parker JA, Drapeau P (2014) Fishing for causes and cures of motor neuron disorders. *Dis Model Mech* 7: 799 – 809

Perez-Garcia MJ, Burden SJ (2012) Increasing MuSK activity delays denervation and improves motor function in ALS mice. *Cell Rep* 2: 497 – 502

Peters OM, Ghasemi M, Brown RH Jr (2015) Emerging mechanisms of molecular pathology in ALS. *J Clin Invest* 125: 1767 – 1779

Pollock S, Kozlov G, Pelletier MF, Trempe JF, Jansen G, Sitnikov D, Bergeron JJ, Gehring K, Ekiel I, Thomas DY (2004) Specific interaction of ERp57 and calnexin determined by NMR spectroscopy and an ER two-hybrid system. *EMBO J* 23: 1020 – 1029

Prudencio M, Belzil VV, Batra R, Ross CA, Gendron TF, Pregent LJ, Murray ME, Overstreet KK, Piazza-Johnston AE, Desaro P, Bieniek KF, DeTure M, Lee WC, Biendarra SM, Davis MD, Baker MC, Perkerson RB, van Blitterswijk M, Stetler CT, Rademakers R *et al* (2015) Distinct brain transcriptome profiles in C9orf72-associated and sporadic ALS. *Nat Neurosci* 18: 1175 – 1182

Ramirez OA, Vidal RL, Tello JA, Vargas KJ, Kindler S, Hartel S, Couve A (2009) Dendritic assembly of heteromeric gamma-aminobutyric acid type B receptor subunits in hippocampal neurons. *J Biol Chem* 284: 13077 – 13085

Roussel BD, Kruppa AJ, Miranda E, Crowther DC, Lomas DA, Marciniak SJ (2013) Endoplasmic reticulum dysfunction in neurological disease. *Lancet Neurol* 12: 105 – 118

Rutkevich LA, Cohen-Doyle MF, Brockmeier U, Williams DB (2010) Functional relationship between protein disulfide isomerase family members during the oxidative folding of human secretory proteins. *Mol Biol Cell* 21: 3093 – 3105

Rutkevich LA, Williams DB (2011) Participation of lectin chaperones and thiol oxidoreductases in protein folding within the endoplasmic reticulum. *Curr Opin Cell Biol* 23: 157 – 166

Sato T, Takahoko M, Okamoto H (2006) HuC:Kaede, a useful tool to label neural morphologies in networks in vivo. *Genesis* 44: 136 – 142

Saxena S, Cabuy E, Caroni P (2009) A role for motoneuron subtype-selective ER stress in disease manifestations of FALS mice. *Nat Neurosci* 12: 627 – 636

Sepulveda FJ, Bustos FJ, Inostroza E, Zuniga FA, Neve RL, Montecino M, van Zundert B (2010) Differential roles of NMDA Receptor Subtypes NR2A and NR2B in dendritic branch development and requirement of RasGRF1. *J Neurophysiol* 103: 1758 – 1770

Silvennoinen L, Myllyharju J, Ruoppolo M, Orru S, Caterino M, Kivirikko KI, Koivunen P (2004) Identification and characterization of structural domains of human ERp57: association with calreticulin requires several domains. *J Biol Chem* 279: 13607 – 13615

Tavender TJ, Bulleid NJ (2010) Molecular mechanisms regulating oxidative activity of the Ero1 family in the endoplasmic reticulum. *Antioxid Redox Signal* 13: 1177 – 1187

Torres M, Medinas DB, Matamala JM, Woehlbier U, Cornejo VH, Solda T, Andreu C, Rozas P, Matus S, Munoz N, Vergara C, Cartier L, Soto C, Molinari M, Hetz C (2015) The protein-disulfide isomerase ERp57 regulates the steady-state levels of the prion protein. *J Biol Chem* 290: 23631 – 23645

Turano C, Gaucci E, Grillo C, Chichiarelli S (2011) ERp57/GRP58: a protein with multiple functions. *Cell Mol Biol Lett* 16: 539 – 563

Turner MR, Hardiman O, Benatar M, Brooks BR, Chio A, de Carvalho M, Ince PG, Lin C, Miller RG, Mitsumoto H, Nicholson G, Ravits J, Shaw PJ, Swash M, Talbot K, Traynor BJ, Van den Berg LH, Veldink JH, Vucic S, Kiernan MC (2013) Controversies and priorities in amyotrophic lateral sclerosis. *Lancet Neurol* 12: 310 – 322

Valenzuela V, Collyer E, Armentano D, Parsons GB, Court FA, Hetz C (2012) Activation of the unfolded protein response enhances motor recovery after spinal cord injury. *Cell Death Dis* 3: e272

Vidal RL, Figueroa A, Court FA, Thielen P, Molina C, Wirth C, Caballero B, Kiffin R, Segura-Aguilar J, Cuervo AM, Glimcher LH, Hetz C (2012) Targeting the UPR transcription factor XBP1 protects against Huntington's disease through the regulation of FoxO1 and autophagy. *Hum Mol Genet* 21: 2245 – 2262

Vogt G, Vogt B, Chuzhanova N, Julenius K, Cooper DN, Casanova JL (2007) Gain-of-glycosylation mutations. *Curr Opin Genet Dev* 17: 245 – 251

Walker AK, Farg MA, Bye CR, McLean CA, Horne MK, Atkin JD (2010) Protein disulphide isomerase protects against protein aggregation and is S-nitrosylated in amyotrophic lateral sclerosis. *Brain* 133: 105 – 116

Walter P, Ron D (2011) The unfolded protein response: from stress pathway to homeostatic regulation. *Science* 334: 1081 – 1086

Wang M, Wen H, Brehm P (2008) Function of neuromuscular synapses in the zebrafish choline-acetyltransferase mutant bajan. *J Neurophysiol* 100: 1995 – 2004

Wang C, Yu J, Huo L, Wang L, Feng W, Wang CC (2012) Human protein-disulfide isomerase is a redox-regulated chaperone activated by oxidation of domain a'. *J Biol Chem* 287: 1139 – 1149

Yang Q, Guo ZB (2015) Polymorphisms in protein disulfide isomerase are associated with sporadic amyotrophic lateral sclerosis in the Chinese Han population. *Int J Neurosci* 18: 1 – 19

Zhao L, Longo-Guess C, Harris BS, Lee JW, Ackerman SL (2005) Protein accumulation and neurodegeneration in the woozy mutant mouse is caused by disruption of SIL1, a cochaperone of BiP. *Nat Genet* 37: 974 – 979